

Seismic anisotropy of mid crustal orogenic nappes and their bounding structures: An example from the Middle Allochthon (Seve Nappe) of the Central Scandinavian Caledonides

Bjarne S.G. Almqvist, Daria Cyprych, Sandra Piazzolo

PII: S0040-1951(21)00327-9

DOI: <https://doi.org/10.1016/j.tecto.2021.229045>

Reference: TECTO 229045

To appear in: *Tectonophysics*

Received date: 1 March 2021

Revised date: 4 August 2021

Accepted date: 1 September 2021

Please cite this article as: B.S.G. Almqvist, D. Cyprych and S. Piazzolo, Seismic anisotropy of mid crustal orogenic nappes and their bounding structures: An example from the Middle Allochthon (Seve Nappe) of the Central Scandinavian Caledonides, *Tectonophysics* (2018), <https://doi.org/10.1016/j.tecto.2021.229045>

This is a PDF file of an article that has undergone enhancements after acceptance, such as the addition of a cover page and metadata, and formatting for readability, but it is not yet the definitive version of record. This version will undergo additional copyediting, typesetting and review before it is published in its final form, but we are providing this version to give early visibility of the article. Please note that, during the production process, errors may be discovered which could affect the content, and all legal disclaimers that apply to the journal pertain.

Seismic anisotropy of mid crustal orogenic nappes and their bounding structures: an example from the Middle Allochthon (Seve Nappe) of the Central Scandinavian Caledonides

Bjarne. S.G. Almqvist¹, Daria Cyprych², Sandra Piazzolo³

1. Department of Earth Sciences, Uppsala University, Uppsala, Sweden
2. Australian Research Council of Excellence for Core to Crust Fluid Systems/GEMOC, Department of Earth and Planetary Sciences, Macquarie University, NSW 2109, Australia
3. School of Earth and Environment, Leeds University, Leeds, United Kingdom

For submission to Tectonophysics, special issue in honor of Adolphe Nicolas

16136 words

18 Figures

4 Tables

Abstract

We report compositional, microstructural and seismic properties from 24 samples collected from the Middle Allochthon (Seve Nappe) of the central Scandinavian Caledonides, and its bounding shear zones. The samples stem both from field outcrops and the continental drilling project COSC-1 and include quartzofeldspathic gneisses, hornblende gneisses, amphibolites, marbles, calc-silicates, quartzites and mica schists, of medium to high-strain. Seismic velocities and anisotropy of P (AV_p) and S (AV_s) waves of these samples were calculated using microstructural and crystal preferred orientation data obtained from Electron Backscatter Diffraction analysis (EBSD). Mica-schist exhibits the highest anisotropy ($AV_p \sim 31\%$; max $AV_s \sim 34\%$), followed by hornblende-dominated rocks ($AV_p \sim 5-13\%$; max $AV_s \sim 5-10\%$) and quartzites ($AV_p \sim 6.5-10.5\%$; max $AV_s \sim 7.5-12.5\%$). Lowest anisotropy is found in calc-silicate rocks ($AV_p \sim 4\%$; max $AV_s \sim 3-4\%$), where the symmetry of anisotropy is more complex due to the contribution to anisotropy from several phases. Anisotropy is attributed to: 1) modal mineral composition, in particular mica and amphibole content, 2) CPO intensity, 3) crystallization of anisotropic minerals from fluids circulating in the shear zone (calc-silicates and amphibolites), and to a lesser extent 4) compositional banding of minerals with contrasting elastic properties and density. Our results link observed anisotropy to the rock composition and strain in a representative section across the Central Scandinavian Caledonides and indicate that the entire Seve Nappe is seismically anisotropic. Strain has partitioned on the nappe scale, and likely on the microstructural scale. High-strain shear zones that develop at boundaries of the allochthon and internally within the allochthon show higher anisotropy than a more moderately strained interior of the nappe. The Seve Nappe may be considered as a template for deforming, ductile and flowing middle crust, which is in line with general observations of seismic anisotropy in mid-crustal settings.

1. Introduction

The understanding of orogeny, or how mountains develop, requires distinguishing between autochthonous and allochthonous tectonic units. For example, tectonic nappes are distinguished in the field based on their distinct composition and the presence of high-strain shear zones bounding them. As seismic data provide key geophysical constraint of the crustal structure at depth, it is important to develop a catalogue of seismic signatures (V_p , V_s , V_p/V_s and anisotropy of V_p and V_s ; e.g., Brownlee et al., 2017; Jung, 2017). In particular, seismic anisotropy is a sensitive indicator for flow and deformation in the Earth, which can be linked to features such as rock fabric, structure (e.g., Okaya et al., 2017) and shear zones (e.g., Jones and Nur, 1982).

Shear zones with widths ranging from mm up to several 10's to 100's of kilometres accommodate relative movement of comparatively rigid surrounding rocks (e.g. White et al., 1980; Ramsay, 1980; Poirier, 1980; Hobbs et al. 1986; Jiang & Williams, 1998; Frederiksen & Braun, 2001; Gueydan et al., 2014; Fossen and Cavalcante, 2017). In brittle shear zones, or faults, deformation is highly localized in distinct narrow zones while ductile crustal shear zones are wider, exhibiting a fabric gradient from host rock to high-strain zone that is, in places, accompanied by strongly developed planar foliation, clear mm to dm scale compositional banding and easy to recognize object lineations (Piazolo & Passchier, 2002), syntectonic metamorphic reactions, development of shape and crystallographic preferred orientations and most commonly finer grain size relative to adjacent rocks (e.g. Ramsay 1980; Celma 1982, Brodie and Rutter, 1987; Law et al. 1990; Piazolo & Passchier, 2002; Svahnberg & Piazolo, 2010). Ductile shear zones develop in a wide range of crustal conditions ranging from 350-750 °C and 0.3-1.2 GPa (e.g., Tullis et al., 1982; Stipp et al. 2002; Passchier & Trouw, 2005) and may form single to anastomosing, that is, interconnected, sets of high strain zones (e.g. Arbaret et al., 2000; Carreras et al., 2010; Svahnberg and Piazolo, 2010). Compositionally, shear zones may be rich in micas such as mica-schists commonly seen in retrograde shear zone within high grade terrains (e.g. Platt & Behrmann, 1986; Selverstone et al. 1991; Raimondo et al. 2011) and biotite rich shear zones developed in response to syntectonic melt-rock interaction (e.g., Piazolo et al. 2020). At higher grade and in mafic rocks, such zones may be amphibole-rich (e.g., Kruse and Stünitz, 1999).

Given their importance in governing crustal deformation, shear zones have been and remain a key target for geophysical imaging, using for example reflection seismology or seismic anisotropy (Jones and Nur, 1984; Burlini et al., 2005; Cholach et al., 2005; Lloyd and Kendall, 2005; Vauchez et al., 2012; Schulte-Pelkum and Mahan, 2014; Almqvist and Mainprice, 2017; Adam et al., 2020; Wrona et al., 2020). Shear zones have been shown to yield seismic signatures or reflections to crustal depths of 30 km, as demonstrated for example by Smithson et al. (1979), Jones and Nur (1984), and more recently by Schulte-Pelkum and Mahan (2014), for the Wind River thrust fault in Wyoming. Rey et al. (1994) have investigated, in some detail, the parameters that give rise to a physical expression of shear zones using reflection seismology. They conclude that the gradient in mylonitization (from protolith to mylonite) and the degree of crystallographic preferred orientation of the main mineral phases is important for the strength and character of the seismic signal. In addition, the common change in composition in terms of rock forming minerals gives rise to seismic property changes distinct to shear zones. For example, amphibole-rich shear zones within high grade, mica poor host rocks will have a distinct signal with high seismic anisotropy, which is accentuated by a strong crystallographic preferred orientation of amphibole (e.g., Ji et al., 1993a, b; Tatham et al. 2008).

Seismic anisotropy is prevalent in the ductile deforming middle and lower crust, below the fracture dominated upper crust. Deep crustal seismic anisotropy has been detected with various methods, including reflection seismology (Hirn et al., 1987), receiver function analysis (Schulte-Pelkum et al., 2005; Audet, 2015; Thybo et al., 2019), surface wave diffraction tomography (Shapiro et al., 2004), and shear wave splitting (e.g., Bokelmann et al., 2013; Sharma et al., 2017; Hu et al., 2020). A growing number of studies have therefore been designed to measure and calculate seismic velocities and anisotropy in different crustal settings, including collisional orogens (e.g., Burlini and Fountain, 1993; Barruol and Kern, 1996; Zappone et al., 2000; Barberini et al., 2007; Lloyd et al., 2011; Almqvist et al., 2013; Erdman et al., 2013; Hacker et al., 2014; Ji et al., 2013; 2015; Cyprych et al., 2017; Kim and Jung, 2020). Based on those studies the presence of foliated, mica-rich rocks is considered among the major sources to middle to lower crustal anisotropy (Brocher and Christensen, 1990; Barruol and Mainprice, 1993b; Shapiro et al., 2004; Lloyd et al., 2009; Dempsey et al., 2011; Erdman et al., 2013; Brownlee et al., 2017; Han and Jung, 2021). Amphibole-bearing middle and lower crustal rocks must also be considered as a major source for seismic anisotropy (Tatham et al., 2008; Ko and Jung, 2015). Monomineralic rocks that tend to

develop strong CPO's in comparison to polymineralic rocks may also act as a source for high anisotropy (Almqvist et al., 2013). However, such rocks are rare, and the addition of a very small modal percent of second phases may decrease anisotropy dramatically, depending on whether the different minerals interfere destructively (e.g., Ward et al., 2012). Another potential source of anisotropy is the compositional banding of layers of minerals with contrasting densities and elastic properties, for example as shown in calculations by Cyprych et al. (2017).

A link between the microstructure of sheared rocks and their seismic properties is inevitable, as minerals and their internal arrangement constitute rocks themselves. This relationship has long been recognized, beginning with key contributions of Vernik (1960), who measured elastic wave speeds along different crystallographic axes in olivine. Subsequently Hess (1964) used these laboratory data in combination with Turner's (1942) study on olivine fabrics, to explain observations of seismic anisotropy in the Pacific Ocean and relate this solid-state mantle flow. A landmark study on relating seismic anisotropy to mineral microstructure and texture was presented by Mainprice and Nicolas (1989), who investigated CPO's developed by quartz, feldspar, pyroxene and amphibole and their role in generating seismic anisotropy by predicting anisotropy through calculations based on mineral constituents and their CPO's. Importantly, this study inferred that prominent lower crustal seismic reflectivity, often observed in continental crust, could at least in part be generated by strongly foliated rocks and consequent seismic anisotropy.

One of the most direct ways of addressing the source of anisotropy in middle and lower continental crust is to model seismic properties based on exposed (outcrop) surface rocks, or drill core and using the mineral composition and texture as model input and analogue for rocks that are currently situated at depth (e.g., Wang et al., 2005; Sun et al., 2012). In the present study, aside from the surface samples, we used drill core material collected from the Collisional Orogeny in the Scandinavian Caledonides (COSC) project, which is a scientific deep drilling project during which ~2.4 km of continuous core was extracted from the Middle Allochthon of the central Scandinavian Caledonides. Research in this project aims to better understand the tectonic history of the Caledonian orogen and help provide insights into other continental collision orogens, such as the Himalaya-Tibet orogen (e.g. Gee et al., 2010; Labrousse et al., 2010; Streule et al., 2010). The drill core recovered from this international drilling project also serves as an excellent opportunity to evaluate the potential sources of seismic anisotropy for a crustal section that represents middle and lower crust that underwent crustal flow and ductile deformation during orogeny.

We present the results of microstructure and texture derived seismic properties of rocks of the Middle Allochthon (Seve Nappe) from the COSC-1 drill core and field samples from selected field sites within the central Scandinavian Caledonides. The aim of this study is to provide texture and microstructure constrained seismic properties, with an emphasis on seismic anisotropy, of a major nappe that hosts and is bound by well-developed shear zones. Seismic velocities and anisotropies are calculated using the ESP Toolbox which takes the spatial distribution and crystallographic orientation of contributing minerals into account (Vel et al., 2016). The mineral orientation and microstructural data were obtained from large area quantitative orientation maps acquired through Electron Backscatter Diffraction (EBSD) analysis. The dataset provides a catalogue of seismic properties to aid the interpretation of geophysical data from heterogeneous deformed mid-crustal rocks in a collisional orogenic setting.

2. Geological setting, sampling strategy and field seismic investigations

2.1 Geological setting

The study area is located in the central part of Scandinavian Caledonides in central Jämtland, Sweden (Figure 1). The site has been recognised as an area of thrusting, with large lateral eastwards displacement of nappes (Gee, 1975; Gee, 1978). The Caledonian front in Jämtland is marked by a sole thrust that dip $1-2^\circ$ westward beneath the orogeny (Gee et al., 2010). Three major allochthonous complexes have been recognised in the area: Upper Allochthon, comprising the Köli Nappe; Middle Allochthon, with Seve, Särvi and Offerdal Nappes; and the Lower Allochthon (Fig. 1). These complexes are made up of rocks derived from the Baltoscandian platform margin, the outer continental shelf and continent-ocean transition zone, and Iapetus oceanic domains (Gee et al., 2010).

The Seve Nappe is divided into three parts, Upper, Middle and Lower, which have each experienced different condition in terms of temperature, pressure and deformation. The Upper Seve Nappe is absent in present study locality, and is therefore not discussed further here. The Middle Seve Nappe, at our study locality, experienced peak pressures exceeding 2.6 GPa and $\sim 700-720^\circ\text{C}$, based on phase equilibrium modelling (Klonowska et al., 2014). After peak pressure conditions, the Middle Seve Nappe experienced decompression melting, at temperatures of $\sim 800-820^\circ\text{C}$ (Klonowska et al., 2014), and granulite facies metamorphic conditions during subsequent nappe emplacement (Arnbom et al., 1980). Geothermobarometry studies of Holmberg (2017), indicate that the Lower Seve Nappe

underwent two metamorphic and deformation events (M1-D1 and M2-D2), where the former event peaked at 0.8-1.3 GPa, 525-695 °C (upper amphibolite facies/lower eclogite conditions), and the subsequent event peaked at 0.7-1 GPa, 450- 550 °C (amphibolite/greenschist grade conditions).

The COSC-1 drilling campaign targeted the lowermost part of Seve Nappe complex and the tectonic contact between the Middle and Lower Allochthon. The Lower Seve Nappe in the area comprises interlayered amphibolites, metasedimentary (quartzofeldspathic) gneisses, calc-silicates, meta-psammities and mica-schist, with minor ultramafics (Figs. 1, 2). The Seve Nappe is underlain by thin slices of the Särvi and Offerdal Nappes thrust over intensely foliated Ordovician and Silurian metasedimentary rocks that belong to the Lower Allochthon (Strömberg et al., 1984; Fig. 1). Figure 1b shows a schematic tectonostratigraphic column with focus on the Middle Allochthon, which can be divided into sub-units of the upper, middle and lower Seve nappe complex and the lowermost Särvi and Offerdal (not shown) nappes (Gee et al., 2020). The Middle Allochthon has two major contacts with the Upper and Lower Allochthon, which occur in general as high-strain zones where deformation has localized during nappe emplacement (Bergman and Sjöström, 1997; Bender et al., 2018; 2019). At the study locality in central Jämtland, the upper Seve nappe complex is not present, and the uppermost sub-unit is considered to belong to the Middle Seve nappe. Several smaller shear zones (m-scale) occur within the Middle Allochthon, and at least one large shear zone (~50 m thick) distinguishes the boundary between the Middle and Lower Seve nappe (Majka et al., 2012).

A schematic lithostratigraphic column and seismic profile (Fig. 2) show two main structural domains interpreted from the drill core and borehole logging. The upper ~1700 m of the borehole is dominated by interlayered gneisses, amphibolites and calc-silicates. Similar lithologies were observed in the nearby outcrops and a nearby quarry (Råsjö quarry; Fig. 3a-c). The rocks are moderately deformed and crop out as intermittent amphibolite and quartzofeldspathic layers ranging with thickness from < 1 cm to greater than 10 m (Fig. 3a-c). This domain is characterized by strong reflectivity, although reflectors are generally laterally discontinuous (Fig. 2). At greater depths, multiple high-strain mylonitic zones, accompanied by mica schist appear (Fig. 2). Towards the bottom of the borehole the volume of the mica-schist increases. High-strained mica-rich units are interbedded with quartzites that are believed to belong to the uppermost Lower Allochthon (Hedin et al., 2014). This domain shows strong and continuous reflectors (Fig. 2).

Nine samples were collected from the COSC-1 drill core at the German Geological Survey (Bundesanstalt für Geowissenschaften und Rohstoffe; BGR) core depository in Berlin, Spandau. Samples were selected to ensure that the main lithologies and their variability in both composition and strain is represented. Fifteen additional samples were collected from the outcrops of the Middle and Lower Seve Nappe, and the contact between Upper and Middle Allochthon (contact between Köli and Seve nappe). These samples were collected from the area surrounding the COSC-1 drill site to provide a more regional representation of samples from the Seve Nappe, including a shear zone at the top contact at the allochthon and a shear zone that separates the Middle from the Lower parts of the Seve Nappe (Fig. 1b). Figures 4-6 present more details on the relative position of the samples within the Seve Nappe, including microstructural appearance. Note that not all samples are shown in Figures 4-6, but rather those that could be placed with some certainty along the tectonostratigraphic profile (Fig. 1b); all samples of the study do however originate from the Seve Nappe and the lowermost part of the Middle Allochthon. During the drilling, a large team of geoscientists described the core in general, on site (cf. lithological column, Fig. 2b). Distinctions were made with regard to general composition (e.g., quartzofeldspathic versus mafic), and structure (granofels, gneiss, schist). Mylonites were defined by very fine grain size and banded appearance.

2.2 Seismic investigations at the study area

A considerable amount of geophysical data has been collected in the scope of the COSC project, with a focus on active seismic experiments (Hedin et al. 2012; 2014; 2016; Juhlin et al., 2016; Simon et al., 2017–2019; Elger et al., 2021). Hedin et al. (2012; 2014) conducted reflection seismic survey, and interpretation of reflections in the Middle Allochthon, which served to help determining the drilling location of the COSC-1 borehole. Hedin et al. (2016) subsequently carried out a detailed reflection seismic survey across the borehole, which led to a detailed view of reflectivity in the upper crust, and an interpretation of structure (Fig. 2a). Elger et al. (2021) related the seismic reflection pattern to compositional layering, although the potential influence of seismic anisotropy was not addressed in their study. An interesting observation that was made from the seismic reflection studies of Hedin et al. (2016) is that the reflectivity pattern changes with depth, within the drilled depth of COSC-1. Towards the lower portion of the borehole (>1700 m) the seismic reflectivity becomes more continuous, likely representing the transition to a thick (>800 m), but anastomosing, shear zone.

Simon et al. (2017; 2019) have investigated the seismic anisotropy in the COSC-1 area, by comparing tomographic imaging with vertical seismic profiling (VSP) carried out in the borehole (Fig. 2b). The conversion to P wave speeds for the two surveys yielded different results, which can only be explained by anisotropic wave speeds, where sub-horizontal P waves obtained by tomographic imaging are up to 10 % faster than vertically propagating waves (VSP; Fig. 2b). Simon et al. (2019) found that in order to interpret seismic reflections and their conversion to depth, it was necessary to consider an anisotropic background medium in the data processing, rather than using an isotropic background medium. Notably the upper crustal portion, which the COSC-1 borehole penetrated, is nearly free of fractures (Tsang et al., 2016) and the observed anisotropy by Simon et al. (2017; 2019) must hence originate from the inherent structure of the rock.

2.3 Laboratory elastic wave speed measurements on COSC-1 samples

In addition to the geophysical Several studies have been carried out with the purpose to characterize the seismic properties of COSC-1 rocks using laboratory measurements (Wenning et al., 2016; Kästner et al., 2020). The studies of Wenning et al. (2016) and Kästner et al. (2020) provide laboratory measurement data of 16 samples of representative rocks from the borehole. Wenning et al. (2016) measured both P- and S-wave speeds of samples, whereas Kästner et al. (2020) focused solely on P-wave speeds. Their measurements were made using cylindrical samples cut along three axes, representing structural orientations where measurements were made parallel to lineation in the foliation plane (X), perpendicular to the lineation but within the foliation plane (Y), and normal to the foliation plane (Z). Measurements were made up to ~260 MPa, at room temperature conditions. Bazargan et al. (in revision) extended these conditions, measuring P- and S-wave speeds on samples of quartzofeldspathic gneiss, biotite gneiss and amphibolite, to 600 MPa and 600 °C, to investigate seismic properties near in-situ conditions in the middle-lower continental crust. Bazargan et al. (in revision) found that seismic anisotropy increased at peak conditions of 600 MPa and 600 °C, compared to solely considering confining pressures up to 600 MPa. For comparison of results collected in this study and laboratory measurements, we provide this in the supplementary material (Fig. S2). Recently, Kästner et al. (2021) investigated seismic anisotropy across the microstructural scale to the borehole scale, using the COSC-1 samples. Their study compared laboratory measurements and textural measurements with anisotropy inferred at borehole scale.

3. Analytical and seismic property calculation methods

3.1. Petrology, mineral chemistry and orientation data

We used polished thin sections cut perpendicular to the foliation (XY) and parallel to the lineation (X). Polarized light-microscopy was used to describe microstructure (grain size, grain shape, and phase distribution) and general deformation structures.

Full crystallographic orientation data were obtained using automatically indexed EBSD patterns acquired with a HKL NordleysNano high sensitivity EBSD detector and indexed using the Aztec analysis software (Oxford instruments). The analysed area of each thin section was larger than 1 cm^2 . The step size was between 10 and $30 \mu\text{m}$. Noise reduction of the raw data was performed following the procedure tested by Prior et al. (2002) and Bestmann and Prior (2003). The detailed description of data processing follows the procedure described in Appendix A of Cyprych et al. (2017). The grain orientation and crystallographic preferred orientation (CPO) data is represented in equal area, lower hemisphere pole figures, with half-width of 15° and cluster size of 1° . The strength of the CPO of each mineral is estimated by comparing the J-index (Bunge, 1982) of the orientation distribution functions (ODFs) derived from all data points using mTEX (<http://mtex-toolbox.github.io/>; Hielscher and Schaeben, 2008). The J-index ranges from unity (corresponding to a completely random fabric) to infinity (a single crystal fabric). In other words, the larger the J-index, the stronger the CPO. Although there is no distinct definition for a strong CPO using the J-index, we consider $J > 3$ as strong J-index for naturally deformed rock. Note that the CPO intensity parameters, such as the J-index, reported in this contribution is based on the area covered by phases throughout an analyzed EBSD section, and not according to counting of one point per grain (ppg). This was done in order to provide a direct comparison between the CPO and calculated seismic properties, since the latter considers the area of the phase, rather than the ppg statistic. However, we do note the calculated number of grains for each section, which generally is well above 100 grains for every analyzed major phase in an EBSD section.

3.2. Calculation of seismic properties

To obtain the bulk homogenised stiffness matrix of polycrystalline rocks an averaging scheme is needed that relates the average elastic strain to average elastic stress of the rock. In case of an aggregate with a CPO, the anisotropy of the elastic properties of each mineral must

be considered, and for each crystallographic orientation the single-crystal properties are rotated (Mainprice, 1990; 2007). Bulk elastic stiffnesses are calculated using ESP Toolbox that applies the asymptotic expansion homogenisation (AEH) method combined with finite element (FE) modelling (Naus-Thijssen et al., 2011b; Vel et al., 2016) together with the classic Voigt-Reuss-Hill homogenisation (Voigt, 1928; Reuss, 1929; Hill, 1952; Mainprice, 1990). The general scheme going from EBSD measurements to calculated seismic properties is shown in Figure 7. The AEH-FE method allows to incorporate the mineral phase boundaries into the calculation, in addition to the classical procedure to calculate seismic anisotropy using only the CPO (Crosson and Lin, 1971; Mainprice, 1990); thus, it allows computation of the effects of phase distribution (e.g., the effect of shape preferred orientation; SPO) and elastic contrast between phases on seismic velocities (e.g., Cyprych et al. 2017).

We calculate seismic properties from EBSD data considering minerals with abundances higher than 1 area %. We used single crystal stiffnesses from several different studies, where references and respective minerals are summarized in Table 1. Alpha quartz (Lakshtanov et al., 2007) was used in calculations where quartz was present in the rock. Although the temperatures expected during metamorphism are likely close to those of the alpha-beta quartz transition at room pressure conditions (573 °C), the transition temperature would be much higher in-situ considering the higher confining pressure in the middle crust.

Seismic anisotropy is defined as $AV_{p,s} = 200[(V_{p,s,max} - V_{p,s,min}) / (V_{p,s,max} + V_{p,s,min})]$, where $V_{p,s,max}$ and $V_{p,s,min}$ are the maximum and minimum values of either the P- or S-wave. Note that for shear wave anisotropy this corresponds to the maximum AVs. The density of the rock is calculated by averaging single crystal densities according to the modal percent of the phases. For the plotting purpose we used the MATLAB Seismic Anisotropy Toolkit (MSAT; Walker and Wockey, 2012).

4. Results

Results are presented in terms of mineral composition (Table 2), texture strength (CPO and J-index; Figs. 8-11, Table 3) and the seismic properties and anisotropy (Figs. 12-16, Table 4). The sample results summarized in Tables 2-4 are grouped according to their composition, the area percentage made up by the different minerals in the EBSD section that was investigated for each sample. The total area investigated for each sample generally comprises a minimum of 1cm² and includes several hundred grains. Supplementary material, section S3 provides the

EBSD maps that were collected in this study, as well as examples (S3.1) of EBSD maps with respect to their location in thin sections. Results for samples are presented according to 1) their position within the tectonostratigraphic unit (Figs. 1b, 2 and 3), 2) their modal mineral composition and 3) their degree of deformation i.e., *medium*- and *high*-strain. The distinction between *high*- and *medium*-strain samples is based on the tightness and planarity of foliation where *high*-strain samples are characterized by highly planar, continuous and tight foliations typical for high strain zones (e.g. Passchier & Trouw, 2005). The category of *medium*-strain encompasses samples with distinct, continuous foliation which are wavy at the mm to cm scale and those that exhibit discontinuous foliations. In general, *medium*-strain samples are internal to the nappes and *high*-strain samples originate dominantly from shear zones that bound the Seve Nappe although some are internal to the nappes itself, originating from a nappe internal shear zone. Description of the results therefore addresses both the comparison of samples of similar composition (rock type) but different CPO intensities, and similar CPO intensity but different composition.

4.1. Rock composition and microstructures

Sample lithology have been defined based on their mineral composition and microstructure, where the groups consist of marble (dominated by calcite), calc-silicates (quartz, plagioclase, K-feldspar and calcite), amphibolite (>70% amphibole), hornblende-gneiss (dominated by mix of plagioclase and amphibole), quartzofeldspathic gneiss (Qfs; quartz, plagioclase and K-feldspar), biotite-gneiss (quartz, plagioclase, K-feldspar and substantial amount of biotite), quartzite (dominated by quartz; sometimes mylonitic) and mica-schist (dominated by muscovite). Sample composition is summarized in Table 2 and representative microstructures are presented in Figs. 4-6.

4.1.1 *Medium*-strain samples

Samples that are noted as *medium*-strain originate from locations outside the *high*-strain shear zones (Fig. 4) that bound the Middle Allochthons, as well as separate the middle and lower parts of the Middle Allochthon (Fig. 1b). Marble (COS13_007) from the upper part of the Middle Allochthon consists of nearly pure calcite, with a lesser amount of quartz. There is a bimodal grain-size distribution of COS13_007, where calcite crystals are up to a few mm, whereas the smaller grains of calcite and accessory phases are less than 100 μm . Calc-

silicates, exemplified by sample COSC13_006, show a much more diverse composition, with nearly equal portions of quartz, plagioclase, K-feldspar and calcite (Table 2). Accessory phases of COSC13_006 consist of diopside, biotite and epidote. Middle Seve Nappe gneisses (SW14_02) are typically quartz dominated, with lesser amounts of feldspar and minor garnet (almandine and pyrope). Quartz ranges in grain-size, from $\ll 1$ mm up to 1 mm. Euhedral garnet occurs as grains of ~ 0.1 mm up to 1 mm.

In the COSC-1 drill core, representing the Lower Seve Nappe, five samples were collected from the top 1700 m of the core (Fig. 5) and include an amphibolite with partially preserved magmatic fabric (COSC_149), amphibolite (COSC_193), two calc-silicates (COSC_243 and 487, respectively), and a quartzofeldspathic gneiss (COSC_403). The amphibolitized gabbro (COSC_149) is composed of hornblende and plagioclase, with minor diopside and biotite. Only weak foliation and lineation are observed (Fig. 5a), and the rock microstructure is close to granoblastic. Hornblende is coarse-grained (from 0.5 up to 4 mm), while plagioclase is finer-grained (< 1 mm). Amphibolite COSC_193 (Fig. 5b) is composed of hornblende and plagioclase with minor quartz. A strong foliation can be seen, which is defined by interlayered hornblende and plagioclase. Hornblende grains are generally smaller than 2 mm. Plagioclase is finer grained with grain size smaller than 0.5 mm. Hornblende exhibits a strong shape preferred orientation (SPO).

The two analysed calc-silicates from the COSC-1 drill core differ in composition. The calc-silicate COSC_243 (Fig. 5c) is composed of calcite, quartz and plagioclase. Calcite is coarser grained than quartz and plagioclase and has a grain size of 1 to 2 mm, while grain size of plagioclase and quartz is < 1 mm. Subgrains and undulose extinction are present in plagioclase and quartz. In contrast, calc-silicate COSC_487 (Fig. 5e) comprises plagioclase, K-feldspar, calcite, diopside, and minor quartz and biotite. A foliation defined with elongated calcite crystals and biotite flakes can be seen (Fig. 5e). Feldspars have grain size of 0.2 to 0.7 mm, calcite of 1 to 3 mm, diopside of 1- to 2 mm and biotite of ~ 1 mm. Calcite shows deformation-induced twins and undulose extinction.

The quartzofeldspathic gneiss COSC_403 (Fig. 5d) is composed of quartz, plagioclase and K-feldspar with minor diopside, biotite and accessory magnetite. A thin layer of coarse-grained (1 to 3 mm) gypsum oriented parallel to foliation has also been observed. However, this gypsum layer was not including in calculations of seismic anisotropy, because it was not deemed representative of the overall composition and microstructure of this sample. The foliation is well defined with biotite flakes. All the minerals are relatively fine-grained (< 1 mm).

4.1.2 *High-strain* (shear zone) samples

Mineral composition and microstructures were studied in samples from three zones along the Seve Nappe, which can be considered *high-strain* zones: 1) the boundary between the Upper and Middle Allochthons, 2) an internal shear zone in the Seve Nappe, and 3) the relatively thick (>700 m) basal, bounding shear zone of the Lower Seve Nappe (Fig. 1). One *high-strain* marble, SC 13_06, was sampled from the top-most shear zone of the Middle Allochthon, and consists essentially of 100 % calcite. It shows a fairly homogenous grain-size (>1 mm), with heavily twinned crystals (Fig. 4c). SC13_08A represent a *high-strain* calc-silicate rock from the same boundary zone, and is dominated by quartz and calcite, with minor amounts of calcite, dolomite, hornblende and mica (Fig. 4a). One sample, MH_09, was taken from the internal Seve Nappe shear zone, separating the Middle from Lower Seve Nappe. This sample consists dominantly of quartz, with lesser amounts of feldspar, biotite and garnet (almandine and pyrope; Fig. 4e), reflecting the composition of Middle Seve Nappe granulites (e.g., SW14_02; Fig. 4d).

The lower section of the COSC-1 drill core, in the Lower Seve Nappe, comprises interlayered hornblende-rich gneisses, mica-schists and meters-thick insets of quartzite. Amphibolite sample COSC_556 (Fig. 6a) is composed predominantly of very fine-grained hornblende and plagioclase (< 0.5 and < 0.2 mm, respectively). This sample is strongly foliated, with foliation defined by SPO of hornblende, and stretched plagioclase and opaques. Plagioclase contains multiple inclusions of zoisite. Hornblende gneiss, COSC_631, exhibits an S-C fabric. The foliation is defined by elongate hornblende grains that surround plagioclase porphyroclasts with fish-like shape (Fig. 6b). Plagioclase porphyroclasts can reach up to 0.6 cm (Fig. 6b) and are partly altered to zoisite. Coarse-grained quartz and calcite occur in porphyroclast strain-shadows.

Mica-schist (COSC_691 in Fig. 6d) is composed of muscovite, quartz, and minor plagioclase, chlorite, opaques and few garnet porphyroclasts. An S-C fabric is present in this sample, and foliation is defined by aligned mica grains. Mica is medium to fine grained (< 1 mm). Garnet porphyroclasts are euhedral to sub-euhedral, and ~ 0.3 cm large. Quartz is locally very fine-grained (<100 μm). The quartzite COSC_664 comprises predominantly quartz, with subordinary plagioclase and chlorite (Fig. 6c). Quartz is fine grained (0.1-1 mm) and shows subgrains and undulose extinction. Plagioclase exhibits deformation twins. Two types of opaque minerals have been observed: stretched aggregates oriented parallel to

foliation and small (0.5 to 1 mm) euhedral to sub-euhedral porphyroclasts (Fig. 6c). Foliation is very well defined with quartz SPO and aligned chlorite grains (Fig. 6c).

4.2 Crystallographic preferred orientation

Results are presented in Figures 8-11 for most representative samples, whereas the texture strength J-index is summarized in Table 3 for minerals of all samples.

4.2.1 *Medium*-strain samples

One sample of marble, COSC13_007, is investigated that originates from a *low* to *medium*-strain domain (Fig. 8a). It shows a weak but fairly well defined CPO, with poles to (0001) clustered normal to the foliation plane. Poles to the mirror prisms (10-10) and a-axes (11-20) are weakly distributed in girdles sub-parallel to the foliation. Quartz show a distinct clustering of (0001) in the foliation plane, but perpendicular to the lineation, whereas (10-10) and (11-20) do not show a clear preferred orientation.

In examined calc-silicates, calcite and plagioclase show similar CPOs (Fig. 9). The poles to (0001) of calcite cluster normal or subnormal to the foliation plane, while poles to (10-10) cluster in the foliation plane (e.g., COSC_243; Fig. 9a). Poles to (001) of plagioclase show clustering normal to foliation whereas poles to (010) cluster normal to lineation (Fig. 9a). For COSC13_006, the poles to (0001) of quartz show a distinct clustering in the centre of the pole figure (Fig. 9b). Other pole figures, for plagioclase, calcite and K-feldspar have much less distinct CPO's. A hint of preferred calcite c-axes can be discerned for this sample (Fig. 9b).

Hornblende in amphibolite COSC_193 shows clustering of poles to (100) normal to foliation and poles to (010) cluster in the direction normal to lineation, in the foliation plane (Fig. 10b). Poles to (001) of hornblende are oriented parallel to lineation (Fig. 10b). Poles to (001) of plagioclase coincide with those of (100) of hornblende, and poles to (100) of plagioclase cluster in the direction of lineation (Fig. 10b). Poles to (010) of plagioclase do not show a clear CPO (Fig. 10b). The plagioclase CPO in the amphibolite COSC_149 is scattered and considerably weaker in comparison to the hornblende CPO (Fig. 10a). The poles to (100) and (001) of hornblende show minor asymmetry (offset) with respect to the lineation (X) and pole to foliation (Z). The J-index values of hornblende and plagioclase are lower for COSC_149 compared to in the amphibolite COSC_193 (J = 2.3 and 1.8, respectively).

For quartzofeldspathic gneiss, plagioclase CPO has a somewhat different pattern to that of plagioclase in amphibolites (e.g., COSC_403; Fig. 11a). Poles to (001) of plagioclase cluster normal to foliation, while those of (100) and (010) do not show a clear CPO, although a weak girdle distribution can be discerned. A CPO is absent for K-feldspar (Fig. 11a). The poles of (0001) of quartz cluster in the foliation plane, normal to lineation, whereas poles to (10-10) show clustering subparallel to lineation (e.g., COSC_403; Fig. 11). Biotite in biotite gneisses (e.g., BQ7.2; Fig. 11b) shows a strong clustering of poles to (001) normal to the foliation, while poles to (100) of biotite cluster parallel to the lineation. Sample SW14_01 shows a very weakly developed CPO for both quartz and plagioclase, although biotite and muscovite have strong CPO with similar patterns as biotite gneiss.

The majority of constitutive minerals of marble, amphibolites, quartzofeldspathic gneiss and calc-silicates from *medium*-strain zone show weak to moderate CPOs (J-index < 3), with exception of biotite and hornblende (J-index > 4; Table 3).

4.2.2 High-strain (shear zone) samples

In the *high*-strain samples, the strength of the CPO increases for most of the minerals (Table 3; Figs. 8-11). Single-phase marble (SC13_06C) show a very strong CPO with c-axes oriented normal to foliation and (10-10) and (11-20) in a girdle parallel to the foliation (Fig. 8c). One *high*-strain calc-silicate has also been investigated, SC13_08A, which contains many phases with varying CPO strengths (Fig. 9c). Hornblende shows the strongest CPO for this sample, with a clear maximum of (100) as pole to the foliation plane. Poles to (010) and (001) also show distinct orientations, where the latter plots parallel to the lineation. The CPOs of hornblende and plagioclase in amphibolites show similar patterns as in low-strain amphibolites, although, a weak asymmetry of the CPO is observed in amphibolite COSC_556, i.e., the poles to (100) and (001) are offset with respect to the lineation and pole to foliation (001) (Fig. 10c). The CPO of hornblende in hornblende gneiss COSC_631, is broadly similar to that of hornblende in the COSC_556, and also shows a similar asymmetric pattern (Fig. 10e). However, COSC_631 shows a girdle distribution of (100) subnormal to the lineation (Fig. 10e), whereas for COSC_556 there is a strong maximum of hornblende (100) subnormal to the foliation (Fig. 10c). Plagioclase CPO in COSC_631 shows multiple single maxima that can be attributed to individual plagioclase porphyroclasts (even though the grain count ~500; Fig. 10e). In quartzite sample COSC_664, poles to (0001) of quartz cluster in the centre of the pole figure, whereas poles to (10-10) are oriented subparallel to lineation (Fig.

11d). The poles to (10-10) of quartz also shows the asymmetry previously observed in hornblende and plagioclase from this domain. The CPO of plagioclase does not show a clear pattern for COSC_664 (Fig. 11d). The CPO of muscovite in mica-schist COSC_691 is characterized by (001) oriented parallel to foliation and poles to (100) clustering in the foliation plane (Fig. 11e). Quartz in this sample shows a weak clustering of (0001) in the centre of the pole figure, and poles to (10-10) do not show a clear pattern (Fig. 11e).

4.3. Calculated seismic properties and anisotropy

Calculated seismic properties from large area EBSD maps are presented in equal area nets for selected samples representative for the different lithologies in Figures 12 and 13. An overview of the results for all samples are compiled in Figure 14, showing the range of V_p and V_s , as well as the AV_p (%) and max AV_s (%). P-wave velocities are generally high in rocks with high density (i.e., hornblende-rich rocks) and lower in rocks with low density (i.e., quartz- and muscovite-rich rocks; Fig. 14). A wide range in anisotropy is observed, with anisotropy generally being higher in samples that show high strain (i.e., originating from shear zones; Fig. 14).

The direction dependent P-, S_1 and S_2 velocities, and shear wave anisotropy (AV_s), and V_{S1} polarization planes, show different patterns for various rock types (Figs. 12-13). Hornblende-rich rocks (COSC_193, 556, 631) show an orthorhombic symmetry of P-wave velocities, with a girdle of fast V_p in the foliation plane, and slow V_p propagating normal to foliation (Fig. 12f, g, i). These amphibolites all have $AV_p > 10\%$, and AV_s ranges from about 8 to 10 %. The distribution of V_{S1} in those rocks is similar to that of V_p . Although not visualized in Figure 12, v_{S2} is slowest in the foliation plane in hornblende-rich rocks. Consequently, strong shear wave splitting is observed in the foliation plane, with V_{S1} polarization planes oriented parallel to the girdle of high AV_s (Fig. 12f, g, i). Sample COSC_149, with the most evident preservation of a primary magmatic fabric, shows a contrasting seismic wave speed pattern compared with other hornblende-rich rocks (Fig. 12e). Notably, it shows a maximum V_p in the foliation plane, but perpendicular to the lineation (both COSC_193 and 556, in Fig. 12f, g, shows maximum V_p parallel to lineation). Also, for V_{S1} , there is a contrast, as COSC_149 (Fig. 12e) show maximum shear wave splitting along the axis of lineation, whereas COSC_193 and 556 (Fig. 12f, g) show high shear wave splitting along the entire foliation plane. In addition, COSC_149 has much lower AV_p (~7 %) and max AV_s (~5 %). Sample HL13_103 (amphibole gneiss) shows similar

microstructure as COSC_149 and has relatively weak seismic anisotropy (Fig. 12h) but has a considerably lower content of hornblende compared to the other amphibolite samples (Fig. 12f-h).

The two calc-silicates show different distribution of seismic velocities. Calc-silicate COSC_487, composed of plagioclase, K-feldspar, calcite, diopside and minor quartz and biotite, shows similar V_p , V_{s1} , V_{s2} and AV_S distribution to the previously described amphibolite COSC_193 (Fig. 12f), but lower overall anisotropy (Table 4). V_p in the calc-silicate COSC_243, composed of calcite, quartz and plagioclase, shows an irregular girdle of fast velocities in the foliation plane, and slow velocities normal to foliation plane (Fig. 12c). V_{S1} , V_{S2} and AV_S show complex patterns with multiple maxima and minima at various angles to foliation and lineation.

Quartzofeldspathic gneiss and quartzite both show a V_p distribution characterized by fast velocities in the sample Y-direction, and slow velocities normal to the foliation plane and parallel to lineation (Fig. 13a, b, d). V_{S1} also shows orthorhombic distribution, with velocity minima that are not related to sample foliation or lineation. AV_S is smallest in the centre of the pole figure (Fig. 13d).

Mica-schist displays dominantly transverse isotropic (or radial) symmetry of V_p and V_{S1} , with slightly orthorhombic distribution of V_{S2} and AV_S (Fig. 13d). V_p and V_{S1} exhibits a girdle of fast velocities in the foliation plane, while V_{S2} is slow in the foliation plane. The shear wave splitting is largest in the foliation plane, with V_{S1} polarization oriented parallel to foliation (Fig. 13e). AV_p and max AV_s are extreme and exceed 30 %. Figure 16 shows a box-and-whisker diagram that compares AV_p and max AV_s for samples have been divided according to high and *medium*-strain. The mica-schist sample COSC_691 clearly stands out in this diagram, with its extreme anisotropy. However, for other samples show a fairly consistent range of AV_p and max AV_s depending on strain, where the difference of median AV_p is ~4 % from *high* to *medium*-strain samples, and ~6 % for max AV_s .

5. Discussion

We initially discuss deformation conditions in terms of temperature and strain. This is followed by the interpretation of the factors controlling seismic anisotropy in the examined samples. Subsequently, we discuss the implications for seismic imaging of anisotropic middle and lower crust and shear zones in particular.

5.1 Deformation condition

In the Lower Seve Nappe all samples show macroscopic *medium-* to *high-*strain features such as clear foliation and lineation development, as well as significant CPOs of the main phases (Figs. 8-11) and grain size reduction (Figs. 4-6) associated with dislocation creep regime. As such, deformation occurred at moderate stresses and deformation temperatures are restricted to >300 °C as dislocation climb must have been possible, considering quartz and calcite. No clear signatures of melt presence are observed, further constraining conditions below the solidus of the rock types studied. Consequently, deformation temperatures in the Lower Seve Nappe must have been between 300 and 750 °C.

Furthermore, deformation temperature can be estimated based on the quartz CPO pattern, as different CPO patterns have been shown to reflect the dominance of specific slip systems at specific temperatures (Law et al., 1990; Law, 2014). Quartz, especially in quartzofeldspathic gneiss and quartzite, shows clustering of the poles to (001) planes in the foliation plane (Figs. 8-10), indicating the activity of prism $\{100\}$ slip, which is expected for temperatures > 500 °C (Mainprice et al., 1986; Stipp et al., 2002; Passchier and Trouw, 2005). Temperatures indicating amphibolite to greenschist facies conditions is further supported by the observed CPO of hornblende, which is common to amphibolites in orogenic regions (e.g., Ji et al., 2013). The observed hornblende CPOs (Fig. 10) can be explained by [001] slip on (100) or (001) typical for lower to mid amphibolite facies conditions at mid crustal levels (e.g., Barruol and Mainprice, 1993a; Ji et al., 1993a). Another potential mechanism for the CPO development of hornblende is through cataclastic flow (e.g., Ko and Jung, 2015; Kim and Jung, 2019), which could operate in combination with dislocation climb or act independently at temperatures ~ 500 °C (Nyman and Law, 1922). The microstructure and texture observed in sample SW14_02 (Fig. 4d) were likely produced during late-stage emplacement of the Seve Nappe. Notably, sample MH_09 originates from a nappe internal shear zone separating Middle from Lower Seve.

5.2 Factors controlling seismic properties and anisotropy in the middle and lower crust

Several factors influence seismic properties and anisotropy in crustal rocks. In previous studies, highest anisotropies of P and S-wave were observed in rocks containing large modal percent of elastically anisotropic phases (e.g., Barruol and Mainprice, 1993b;

Lloyd et al., 2009; Dempsey et al., 2011; Lloyd et al., 2011; Naus-Thijssen et al., 2011; Erdman et al., 2013; Ji et al., 2015; Han and Jung, 2021). Especially mica and amphibole can significantly contribute to the overall anisotropy of the rock (Aleksandrov and Ryzhova, 1961; Ryzhova et al., 1966; Vaughan and Guggenheim, 1986). However, if these anisotropic minerals are oriented randomly in the sample volume, single crystal elastic anisotropy will not yield an overall anisotropy of the polymineralic aggregate. Thus, the presence of CPO is crucial for the seismic properties of natural rocks, in the absence of a preferred orientation of microcracks (Mainprice and Nicolas, 1989).

Notably, the seismic properties of nearly pure marbles reflect the CPO of calcite. Sample SC13_06C (Fig. 12b) shows $AV_p \sim 16\%$, and $max AV_s \sim 11\%$, which are very high; calcite is considerably anisotropic (Chen et al., 2001). However, marble CPO's can decrease significantly in the presence of second phase minerals, including quartz (see discussions of Khazanehdari et al., 1998 and Almqvist et al., 2013). Multi-mineral samples are likely to be much weakly anisotropic, which is reflected in generally calc-silicates of this study.

We can observe these relationships by examining the predicted seismic anisotropy of three hornblende-rich rocks for the COSC-1 core, i.e. COSC_149, 193 and 556 (Fig. 12e-g). Their seismic properties, in particular anisotropy, are primarily controlled by the CPO of hornblende and secondarily by differences in mineral composition (i.e., amount of amphibole; Fig. 16). With the exception of sample COSC_149, V_p is lowest sub-parallel to the poles to (100) of hornblende and fastest sub-parallel to the poles to (001) (Fig. 10a-c, 12f-h). Note that the maximum V_p in hornblende is parallel to [001], which is offset with respect to the pole to (001) because of its monoclinic crystal symmetry. In hornblende β (angle between crystal a - and c -axes) shows a range of variation from $12\text{--}34^\circ$ (Deer et al., 2013) and based on the EBSD solution fit for data in our study $\beta = 105.2^\circ$. Hence the V_p fast and slow axes are only sub-parallel to the poles of (100) and (001). In addition, the minimum AV_s corresponds to (100), while the largest AV_s is observed in a girdle containing (010) and (001) orientations (Fig. 10, 12c), characteristic for amphiboles (Barruol and Mainprice, 1993b; Ji et al., 1993a, b). The COSC_149, 193 and 556 amphibolites have comparable mineral compositions and densities (Table 2), but evidently different predicted seismic anisotropy (Fig. 12e-g). We attribute these differences in anisotropy to different strength of the CPO of hornblende as quantified by the J-index and apparent in the pole figures. The difference in CPO in this case is attributed to different amount of strain accommodated by each sample, as inferred from the grain size reduction and fabric development (Fig. 6). Thus,

increasing anisotropy can carry possible information about the degree to which the rock has been strained.

Plagioclase in hornblende-rich rocks will also affect the overall seismic properties. Plagioclase is considered elastically anisotropic (Aleksandrov and Ryzhova, 1962; Ji and Mainprice, 1988; Brown et al., 2006), however, it has a contrasting seismic signature to hornblende. Plagioclase is characterized by slow P-wave velocities parallel to poles to (100) and (001), and fast velocities in the direction of pole to (010) (Aleksandrov and Ryzhova, 1962; Brown et al., 2006). Thus, V_p in the (001) will negatively correlate with V_p of hornblende. A very weak CPO of plagioclase limits its possibility of decreasing the overall seismic anisotropy within the amphibolites. Nevertheless, as shown by the amphibole gneiss COSC_631, a strong CPO of plagioclase porphyroclasts can result in a noticeable decrease in the overall anisotropy (Figs. 10e, 12i). Plagioclase CPO patterns vary among the amphibolites and the sample set in general. Most commonly, the poles to (001) plot normal to foliation (e.g., COSC_243, SC13_08A, COSC_193, COSC_403; Figs. 9c, 10b, 11a). The (100) and (010) are generally weak, but in a few cases, there are maxima of (010) normal to foliation (e.g., COSC_556, HL13_103; Fig. 10c, d) and (001) poles within the foliation plane (e.g., COSC_631). We do not address the formation processes, in terms of plastic deformation mechanisms, because of the large number of slip-systems for plagioclase and possibilities for superposed/interacting magmatic and metamorphic textures during deformation (Satsukawa et al., 2015).

Additionally, it is important to consider the composition of plagioclase when considering its impact on the seismic properties, including anisotropy. In our study we used the elastic stiffness tensor of albite (Brown et al., 2016) for all samples, which was constrained by best fit to the EBSD data. However, by increasing Ca-composition it is apparent that bulk V_p tend to increase, because of higher elastic stiffness in Ca-rich plagioclase (Brown et al., 2016). An example of the effect of plagioclase composition is provided in the online supplementary material (S4.1), where the seismic properties are compared for a number of plagioclase-rich samples. Notably, the largest differences are observed in the most plagioclase rich sample (HL13_103 in Table 4), corresponding to a decrease in AV_p of ~1.5 % and increase in bulk V_p of ~200 m/s (from albite to labradorite composition; online supplementary material, S4.1). The differences in shear wave speed (V_{s1} and V_{s2}) and anisotropy are essentially negligible.

The quartzite samples, containing more than 70 % quartz (SW14_11, SW14_02, MH_09, COSC_664; Fig. 4d, e, Fig. 6c), show considerable anisotropy ranging from AV_p

6.5 to 10.7 % (Table 4). The high anisotropy is largely due to the strong CPO of quartz. In case of quartzite (e.g., COSC_664; Figs. 6c, 11d, 13d) and Qfs gneiss (e.g., COSC_403; Figs. 5d, 11a, 13a), the seismic anisotropy is caused by both CPO strength and composition. The orthorhombic Vp pattern observed in these samples (Fig. 13a, d) results from the c-axis clustering of quartz. As quartz exhibits a strong CPO, the resultant seismic signal has the same pattern. In quartzofeldspathic gneiss, the orthorhombic signature of Vp originating from quartz is slightly modified by the presence of feldspars (Fig. 11a, 13a). However, due to the difference in CPO strength of quartz in both samples (Fig. 11a, d), quartz-feldspar gneiss (COSC_403) shows higher anisotropy than quartzite (COSC_664). In addition, the anisotropy of the former might be slightly increased by the presence of few modal percent of the highly elastically anisotropic biotite (Table 2), as the fast Vp direction in biotite lies in the foliation plane.

The highest anisotropy observed in this study was calculated for mica schist (COSC_691), which originates from the large modal percent of muscovite and its strong CPO (Fig. 13e, 14, 15, 16). Muscovite is one of the most anisotropic minerals that commonly occur within the crust and it is characterized by fast P-wave propagation parallel to a- and b-axis of the crystal, and slow P-wave propagation parallel to c-axis (pole to (001); Vaughan and Guggenheim, 1986). The S-C fabric observed in COSC_691 (Fig. 6), similar to crenulation cleavage, can in theory decrease the CPO and anisotropy of mica schist (Naus-Thijssen et al., 2011a). However, despite the presence of S-C fabric in this sample, the predicted anisotropy is very high (>30 % AVp and max AVs; Fig. 13e). Similar anisotropies in mica rich rocks have been reported in previous studies (e.g., Lloyd et al., 2009; Erdman et al., 2013; Ji et al., 2015; Han and Jung, 2021).

The individual roles of amphibole and mica (considering the total amount of biotite plus muscovite) can be evaluated by considering AVp and AVs as a function of modal composition. This relationship is shown in Figure 15; AVp and AVs correlate positively with the amount of amphibole and mica. In particular the amount of mica is clearly positively correlated, although it is considerably influenced by one data point that represent the mica-schist sample (COSC_691). It is interesting to note that slope of linear fits to the data of amphibole and mica differs, which is a consequence of the strength of CPO, but also of the inherent elastic anisotropy of each mineral. Micas are considerably more anisotropic than amphibole (Aleksandrov and Ryzhova, 1961; Vaughan and Guggenheim, 1986). The linear fit to AVp and AVs as a function amphibole content is less evident, although it is clear that a higher amount of amphibole will generally yield a higher degree of AVp and max AVs.

However, even when amounts of mica and amphibole are low, the rocks can be considered anisotropic. Other minerals, such as calcite, quartz and plagioclase do contribute to the overall anisotropy, although to lesser extent than amphibole and micas.

The low anisotropy in calc-silicates is more challenging to interpret because these rocks are composed of many minerals of contrasting elastic properties (Table 2, Fig. 12c, d). The calc-silicate COSC_487 (Fig. 5e) shows strong signature of plagioclase (001), (010), and diopside (100) (Collins and Brown, 1998). In contrast, the velocity patterns in calc-silicate COSC_243 (see section S4 in supplementary material) are controlled by the elastic properties of calcite (0001; e.g., Chen et al., 2001). Their low V_p and V_s anisotropies originate from weak CPOs (Fig. 9) that might originate from low strain as well as interference in the directional seismic properties of constitutive minerals. The two marble samples analyzed in this study (COSC13_007 and SC13_06C) show markedly different seismic signature (Fig. 12a, b), even though they are both dominated by calcite. Sample SC13_06C contains 100 % calcite and has a fairly strong J-index ($J = 5.0$), which leads to a substantial seismic anisotropy (Fig. 8b, Table 3, 4). However, COSC13_007 has a much weaker calcite J-index ($J = 2.1$), and presence up to 10 % quartz and minor plagioclase, which may act to inhibit the development of a strong CPO in this sample (Fig. 8a, Table 3, 4).

5.3 Seismic signature of allochthonous units and high-strain shear zones

5.3.1 Anisotropy due to crystallization of anisotropic phases (calc-silicates and amphibolites)

Crystallization of minerals in a shear zone in the presence of crustal fluids is another potential mechanism by which it is possible to generate anisotropic rocks (Berger and Stünitz, 1996; Kruse and Stünitz, 1999; Mahan, 2006). Calc-silicate rocks form through metasomatic reactions in the presence of Ca-rich fluids that may originate from limestone or marble, and their end products typically include diopside and wollastonite (Bucher and Grapes, 2011). There is relatively little wollastonite present in the calc-silicates of this study, although significant amounts of diopside can be present as well as abundant calcite (Table 2). Calc-silicates are fairly common throughout the Seve Nappe, although they have been seldomly studied for their seismic properties.

Most calc-silicate samples that are presented in this study show fairly weakly developed anisotropy, and it is clear that this group of rocks contribute the least to anisotropy through the entire allochthonous unit. The most anisotropic calc-silicate sample (SC13_08A; Fig.

12d), display a distinct symmetry of anisotropy, with high wave speeds parallel to the foliation plane (with $AV_p \sim 7\%$ and max $AV_s \sim 9\%$). This sample displays an extremely strong amphibole CPO, making up just less than 10 % of the modal mineral composition (Table 2), which is main source for anisotropy in this sample. In addition, there are less strong CPO's of calcite, plagioclase and dolomite that contributes in part to the seismic anisotropy in this sample (Fig. 9c).

5.3.2. Enhanced anisotropy due to compositional banding?

Compositional banding will play a role for seismic anisotropy under certain conditions (Cyprych et al. 2017). Notably, there needs to be a considerable contrast in elastic constants and density between minerals that make up the compositional bands. Moreover, the thickness of a sequence of banding should be considerable, including many seismic wavelengths. Effects of compositional layering with contrasting elastic properties depend largely on the layer thickness with respect the wave length (and frequency), and ultimately on the scale that is considered (e.g., Marion et al., 1994; Liu and Scarmitt, 2006). On a microstructural scale, compositional banding is observed for a few of the samples investigated in this study. Notably, sample BQ7.2 (biotite gneiss) shows a regular banding of feldspar and biotite. The CPO of biotite in BQ7.2 is strong (Fig. 11b) and with a modal composition just below 20 % (Table 2), it is likely that these two factors largely explain the source of anisotropy for this sample. Nevertheless, if there is a significant elastic and density contrast between the micro-scale mineral bands, it can affect both the symmetry and strength of anisotropy (e.g., Cyprych et al., 2017).

Figure 17 illustrates the difference in predicted AV_p and $MaxAV_s$, by comparing calculations using solely the Voigt-Reuss-Hill (VRH) average and the combined VRH-AEH average. The comparison shows that generally, independent of lithology, there is an increase in anisotropy using the combined VRH-AEH calculation, although often this increase is $<1\%$ AV_p or $MaxAV_s$. In some case there is a smaller, negative, difference between the two calculations, although $<1\%$. It is interesting to note that the quartz-feldspar dominated gneisses show the most consistent AV_p and $MaxAV_s$, with an increase of $\sim 0.5-1\%$ when comparing the VRH and the combined VRH-AEH. The largest absolute difference is observed for $MaxAV_s$ of mica-schist COSC_691, which is $\sim 2.25\%$ (Fig. 17).

Compositional banding is also evident on a larger scale in the Seve Nappe. Alternating layers of quartzofeldspathic gneiss and amphibolite occur on cm up to tens of meters in the upper 1700 m of the COSC-1 borehole. Given a large enough contrast in terms

of density and elastic properties, such layering may itself be source of seismic anisotropy (Backus, 1962) and strong seismic reflections. It is possible to perceive in this case that if these layers are inherently anisotropic, seismic anisotropy could be amplified if layer anisotropy and inherent anisotropy interfere constructively. Alternatively, anisotropy could be diminished, if the layer and inherent anisotropies destructively interfere.

5.3.3. Strain distribution in shear zones and seismic anisotropy

Strain partitioning may play a role in the development of the basal shear zone of the Middle Allochthon as textural contrasts between quartzite COSC-1_664 and mica-schist COSC-1_691 are apparent (Fig. 6c, d). COSC_664 is located in the domain of the shear zone and composed dominantly of quartz, a quartzite (metamorphosed sandstone). A moderately strong c-axis maximum has developed in this sample, but the overall CPO and microstructural appearance of this sample indicates that it has experienced relatively low strain in comparison to other samples from the shear zone. In comparison, COSC_691 shows a very weak CPO of quartz, but very strong CPO of muscovite (which is absent in COSC_664). The grain count for the quartz is large enough (>3000) for COSC_664 and COSC_691, indicating that the CPO and J-index is statistically reliable (Fig. 11d, e). Strain is often localized in mica-schist, due the highly non-linear rheology of mica (Kronenberg et al., 1990; Montési, 2013). The CPO pattern of mica (Fig. 11e) suggests the [100](001) glide to be dominant mode of deformation (Ji et al., 2015).

Quartz in quartzite (SW14_11, SW14_02, MH_09, COSC_664) shows relatively weak CPO when compared to other quartz-bearing rocks from high-strain units. As quartz grain-size is too coarse (0.1-1 mm) in COSC_664 to suspect grain boundary sliding (e.g., Fliervoet et al., 1997), we speculate that the relatively weak CPO in quartz may be due to the fact that quartzite accommodated less strain than mica-rich rocks (COSC_691). Thus, although strain increases towards the bottom of the drill hole, strain within the *high*-strain zone appears to be heterogeneously distributed. However, the microstructures observed for COSC_664 (Fig. 6e) are similar to regime 3 of Hirth and Tullis (1992), indicating that dynamic recrystallization occurs by grain boundary migration and subgrain rotation. Deformation conditions that lead to these microstructures suggest low strain-rate, and/or higher temperature during recrystallization. Importantly, in regime 3 quartz reach a steady-state recrystallization at relatively low strain. A counter argument therefore to strain partitioning is the relatively low strains needed to achieve steady-state dynamic recrystallization of the quartz microstructure (regime 3, Hirth and Tullis, 1992). If quartzites in the basal shear zone (COSC_664) achieved

a steady-state microstructure at relatively low strain it is challenging to invoke its role in strain partitioning as it may not be possible to indicate to what degree the quartzites have been strained.

Quartz CPO patterns are similar for samples throughout the *high*-strain zone, suggesting that temperatures were relatively uniform throughout the whole Lower Seve Nappe section. Strain increases with depth, and it is distributed, and does not localize in a narrow horizon. This is supported by the mineral assemblages, which do not change significantly within the drill core for rock of similar bulk composition, observed at various depths (e.g., amphibolites and quartzofeldspathic gneisses; Figs. 10 and 11). Much of the bottom-most few hundred meters of the drill core consists of anastomosing bands with contrasting quartz (quartzite) and mica dominated layers (Fig. 6), varying in thicknesses from mm to >1 m. The effective seismic properties of the shear zone would thus, in part at least, be controlled by the averaged properties of mica- and quartz-rich layers. Importantly, the directional dependence of V_p does not destructively interfere (see discussion of Ward et al., 2012), as the highest wave speeds are observed in the foliation plane and slow velocities normal to foliation. The averaged V_{s1} polarization is, however, more complex (Fig. 13d, e) and show different polarization patterns.

For amphibolites, the increasing strength of the CPO of hornblende (Fig. 10a-c), accompanied by the grain size reduction from samples COSC_149, through 193, to 556, i.e. towards the bottom of the borehole (Fig. 5, 6), may suggest deformation in the dislocation creep regime, with strain gradually increasing towards the *high*-strain zone. These three samples have a similar composition, with hornblende modal content varying from 58 to 72 % (Table 2), thus the difference in CPO strength is rather attributed to deformation conditions, i.e., strain compared to compositional variations (e.g., Kim and Jung, 2019). Other than the influence of strain, factors such as differential stress and temperature could influence CPO development in amphibolites (e.g., Ko and Jung, 2015).

Sample SW14_02 (from the Middle Seve Nappe; Fig. 1; supplementary S.5) shows contrasting seismic properties compared to COSC_664 (Fig. 13d), in that it shows considerable seismic anisotropy ($AV_p = 10.7\%$; $\max AV_s = 12.3\%$), even though these two samples have very similar modal mineral composition. SW14_02 has developed strong quartz, plagioclase and K-feldspar CPO's (Table 3), which is the source for the high AV_p and AV_s , hence illustrating that rocks with low mica and amphibole contents can still be the source of significant seismic anisotropy. In this case, the conditions of deformation allowed for development of strong CPO in a sample that did not contain mica or amphibole.

5.3.4. What seismic signature can we expect in shear zones and the allochthonous unit?

The strength of anisotropy of the ductile flowing crust is a consequence of 1) the degree of strain that the rocks have experienced and resulting microstructure (i.e. CPO, SPO/mineral banding) (Fig. 16) and 2) the modal composition of mainly mica and to a lesser extent amphibole and other elastically anisotropic minerals (Fig. 15). Although this is not a new finding, we have here been able to study the relationship between both degree of strain and the effect of mineral composition across a crustal-scale structure. Clearly, a shear zone where the mica modal composition is high is a likely candidate both for generating seismic anisotropy, as well as seismic reflections considering active seismic reflection survey. The COSC-1 reflection seismic survey presented by Hedin et al. (2016) shows distinct continuous reflections at ca 2.1 to 2.2 km depth (Fig. 2a). Drill core retrieved from these depths show an increasing amount of mica-schist, which is the likely source lithology for generating the seismic reflectivity. AVp and AVs exceed 20 % in this case, considering both laboratory measurements (e.g., Wenning et al., 2016; Kästner et al., 2020) and predicted velocities based on microstructural and textural constraints (e.g. Figs. 13e and Fig. 16).

Schulte-Pelkum and Mahan (2014) have addressed the limit of detection of crustal scale shear zones, and note that for detection using receiver function analysis only a few percent seismic anisotropy is needed in contrast with the surrounding host rock. However, a significantly thick section is required (~2 km in the study of Schulte-Pelkum and Mahan, 2014) in order to resolve the shear zone. The entire section of the Seve Nappe (Middle Allochthon) represents an anisotropic unit, whose thickness varies somewhat depending on locality, but will amount to at least 4 km at study locality (considering the nearly vertical 2.5 km borehole depth and a >1 km height difference of the nearby mount Åreskutan). Strain has partitioned within the Seve nappe itself, by dividing a ductile flowing middle to lower crust, with intermittent shear zones separated by less strained regions (although still showing evidence of considerable deformation). When the entire crustal segment is considered it is possible to discern considerable anisotropy. Such may be the case in many middle and lower crustal sections where deformation has taken place or is currently taking place (e.g., Shapiro et al., 2004; Schulte-Pelkum et al., 2005).

In the present study, all seismic projections presented have similar symmetry, i.e., fast axis in the foliation plane and generally parallel to the mineral stretching lineation and a slow axis normal to the foliation plane (Figs. 12 and 13). This configuration of seismic anisotropy, although varying somewhat in magnitude in regards to absolute wave speeds and anisotropy,

preserves the same symmetry of anisotropy throughout the whole Middle Allochthon. Figure 18 provides a schematic cross-section of the seismic properties (AV_p , AV_s and range in V_p) across the Middle Allochthon. There is a general coincidence between high-strain zones high seismic anisotropy, occurring at the upper and lower bounding contacts of the allochthon, as well as internal to the Middle Allochthon, separating middle and lower parts of the Seve Nappe. Note that the transition from middle to upper part of the Seve Nappe is missing in our study area and this is indicated by an area labelled “section break” in Figure 18. The fast axis of V_p coincides generally with the transport direction of the nappe on both a local scale (e.g., shear zones) and at a tectonostratigraphic scale. The slow axis of V_p is generally oriented normal to the allochthon bounding contacts. The Middle Allochthon of the Central Scandinavian Caledonides could hence be considered as a template for deforming, ductile and flowing middle crust, which appears to be in line with general observations of seismic anisotropy in current-day mid-crustal settings.

6. Conclusions

We modelled seismic properties of a suit of representative samples from the COSC-1 drill core and outcrop localities in the region around the borehole. Sampling covered much of the Middle Allochthon and its bounding shear zones to the Upper and Lower Allochthons. Samples were divided into structural domains of: (1) *medium*-strain, composed of interlayered amphibolite and quartz-feldspar-rich lithologies, and (2) *high*-strain that comprises amphibolites and gneisses (sometimes mylonitic), and interbedded *high*-strain mica-schist and *medium*-to-*high* strain quartzite. Marble and calc-silicate were also part of the sample set, and displayed both *high*- and *medium*-strain. *High*-strain samples originate from shear zones, whereas *medium*-strain samples represent rocks that deformed in a mid-crustal setting, but internal to the nappe (and not from a shear zone).

A large range in anisotropy was identified, which could be attributed to the presence of highly anisotropic minerals, i.e., hornblende and mica that exhibit strong CPO, as well as the degree to which the rock has been strained. The largest anisotropy is found in single-phase dominated lithologies that are rich in mica and amphibole. These results agree with previously published seismic properties of similar rocks from other collisional orogens. Quartzites also show significant seismic anisotropy (AV_p from 6.5 to 10.5 %; max AV_s from 7.5 to 12 %). To a lesser extent, compositional banding can affect seismic anisotropy, which

has been less commonly discussed as a source for seismic anisotropy in the lower and middle crust.

Importantly, the entire Seve Nappe (Middle Allochthon) is anisotropic, independent of source rock/mineral composition and degree of strain, even though there is a lower range of anisotropy (~5-10 %) in *medium*-strain regions. The Middle Allochthon of the Scandinavian Caledonides can hence be used as a sort of template for ductile deformed mid- and lower crust. Although it is not exactly transferable to other crustal sections, it is generally transferable and indicates that much of the (flowing) mid and lower crust is inherently anisotropic.

Acknowledgements

The EBSD data were obtained using instrumentation funded by DEST Systemic Infrastructure Grants, ARC LIEF, NCRIS, industry partners and Macquarie University. All the analyses were performed at the Geochemical Analysis Unit (GAU), in the Department of Earth and Planetary Sciences at Macquarie University, Australia. We thank David Adams for his support during SEM-based analyses and thank the ARC Centre of Excellence for Core to Crust Fluid Systems (CCFS, <http://www.ccfs.mq.edu.au>) for supporting B. Almqvist through a CCFS Visiting Researcher grant. We acknowledge the COSC-1 on-site team for their excellent core logging and core handling. We are very grateful to the valuable reviews of Haemyeong Jung, Kevin Mahan and an anonymous reviewer, as well as comments from the editors, Philippe Agard and Katsuyoshi Michibayashi, which significantly help improve the manuscript. Drilling operations of the COSC-1 project was financed by the International Continental Scientific Drilling Program (ICDP) and the Swedish Research Council (VR, grant 2013-94). This work was supported by the Australian Research Council (project DP120102 and FT1101100070) and the Swedish Research Council (VR, grants 2012-04449 and 2018-03414).

References

Adam, L., Frehner, M., Sauer, K., Toy, V., Guerin-Marthe, S. 2020. Seismic anisotropy and its impact on imaging the shallow Alpine Fault: An experimental and modeling perspective. *J. Geophys. Res.* 125, doi:10.1029/2019JB019029.

- Alexandrov, K. S., Ryzhova, T.V. 1961. Elastic properties of rockforming minerals. II. Layered silicates, *Izv. Acad. Sci. USSR Geophys. Ser., Engl. Transl.*, 12, 1165–1168.
- Almqvist, B.S.G., Hirt, A.M., Herwegh, M., Ebert, A., Walter, J.M., Leiss, B., Burlini, L. 2013. Seismic anisotropy in the Morcles nappe shear zone: Implications for seismic imaging of crustal scale shear zones. *Tectonophysics* 603, 162-178.
- Almqvist, B.S.G., Misra, S., Klonowska, I., Mainprice, D., Majka, J. 2015. Ultrasonic velocity drops and anisotropy reduction in mica-schist analogues due to melting with implications for seismic imaging of continental crust. *Earth Planet. Sci. Lett.* 425, 24-33.
- Almqvist, B.S.G., Mainprice, D. 2017. Seismic properties and anisotropy of the continental crust: Predictions based on mineral texture and rock microstructure. *Rev. Geophys.* 55, 367-433, doi:10.1002/2016RG000552.
- Arbaret, L., Burg, J.-P., Zeilinger, G., Chaudhry, N., Hussain, S., Dawood, H. 2000. Pre-collisional anastomosing shear zones in the Kohistan arc, NW Pakistan. *Geol. Soc. London Spec. Pub.* 170, 295-311.
- Arnbom, J.-O. 1980. Metamorphism of the Sveve Nappes at Åreskutan, Swedish Caledonides. *Geologiska Föreningen i Stockholm Förhandlingar* 102, 359-371.
- Audet, P. 2015. Layered crustal anisotropy around the San Andreas Fault near Parkfield, California. *J. Geophys. Res.* 120, 2527-2543.
- Backus, G.E. 1962. Long-wave elastic anisotropy produced by horizontal layering. *J. Geophys. Res.* 67, 4427-4440.
- Barberini, V., Burlini, L., Zappone, A. 2007. Elastic properties, fabric and seismic anisotropy of amphibolites and their contribution to the lower crust reflectivity. *Tectonophysics* 445, 227-244.
- Barruol, G., Mainprice, D. 1993. A quantitative evaluation of the contribution of crustal rocks to the shear-wave splitting of teleseismic SKS waves. *Phys. Earth. Planet. Int.* 78, 281-300.
- Bender, H., Ring, U., Almqvist, B.S.G., Grasemann, B., Stephens, M.B. 2018. Metamorphic zonation by out-of-sequence thrusting at back-stepping subduction zones: sequential accretion of the Caledonian Internides, central Sweden. *Tectonics* 37, 3545-3576, doi:10.1029/2018TC005088.

- Berger, A., Stünitz, H. 1996. Deformation mechanisms and reaction of hornblende: examples from the Bergell tonalite (Central Alps). *Tectonophysics* 257(2-4), 149-174.
- Bergman, S., Sjöström, H. 1997. Accretion and lateral extension in an orogenic wedge: Evidence from a segment of the Sve-Köli terrane boundary, central Scandinavian Caledonides. *J. Struct. Geol.* 19, 1073-1091.
- Bokelmann, G., Qorbani, E., Bianchi, I. 2013. Seismic anisotropy and large-scale deformation of the Eastern Alps. *Earth Planet. Sci. Lett.* 383, 1-6.
- Brocher, T.M., Christensen, N.I. 1990. Seismic anisotropy due to preferred mineral orientation observed in shallow crustal rocks in southern Alaska. *Geology* 18, 737-740.
- Brodie, K. H., Rutter, E. H. 1987. The role of transiently fine-grained reaction products in syntectonic metamorphism: natural and experimental examples. *Can. J. Earth Sci.* 24, 556-564.
- Brown, J.M. and E.H. Abramson 2016. Elasticity of calcium and calcium-sodium amphiboles. *Phys. Earth Planet. Int.* 261,161-171.
- Brown, J.M., Angel, R.J., Ross, N.L. 2016. Elasticity of plagioclase feldspars. *J. Geophys. Res.* 121, doi:10.1002/2015JB12736.
- Brownlee, S.J., Schulte-Pelkum, V., Raj, A., Mahan, K., Condit, C., Orlandini, O.F. 2017. Characteristics of deep crustal seismic anisotropy from a compilation of rock elasticity tensors and their expression in receiver functions. *Tectonics* 36, 1835-1857.
- Bucher, K., Grapes, R. 2011. *Petrogenesis of Metamorphic Rocks*. 8th edition. Springer Verlag Berlin-Heidelberg, 422 pp.
- Burlini, L., Fountain D. 1993. Seismic anisotropy of metapelites from the Ivrea-Verbano zone and Serie dei Laghi (northern Italy). *Phys. Earth Planet. Int.* 78, 301-317.
- Burlini, L., Arbaret, L., Zeilinger, G., Burg, J.-P. 2005. High-temperature and pressure seismic properties of a lower crustal prograde shear zone from the Kohistan Arc, Pakistan. *Geol. Soc. London Spec. Pub.* 245, 187-202.
- Carreras, J. Czeck, D.M., Druguet, E., Huddleston, P.J. 2010. Structure and development of an anastomosing network of ductile shear zones. *J. Struct. Geol.* 32, 656-666.
- Celma, A. G. 1982. Quartz of C-Axis fabric variation at the margins of a shear zone developed in shists from cap de Creus (Spain). *Acta Geologica Hispanica*, 137-149.

- Chai, M., Brown, J.M. and L.J. Slutsky (1997), The elastic constants of a pyrope-grossular-almandine garnet to 20 GPa, *Geophysical Research Letters*, 24, 523-526.
- Chen, C.-C., Lin, C.-C., Liu, L.-G., Sinogeikin, V., Bass, J.D. 2001. Elasticity of single-crystal calcite and rhodochrosite by Brillouin spectroscopy. *Am. Min.* 86, 1525-1529.
- Cholach, P.Y., Molyneux, J.B., Schmitt, D.R. 2005. Flin Flon belt seismic anisotropy: Elastic symmetry, heterogeneity, and shear wave splitting. *Can. J. Earth Sci.* 42, 533-544.
- Collins, M.D., Brown, J.M. 1998. Elasticity of an upper mantle clinopyroxene. *Phys. Chem. Min.* 26, 7-13.
- Cook, A.C., Vel, S.S. 2013. Multiscale thermopiezoelectric analysis of laminated plates with integrated piezoelectric fiber composites. *Eur. J. Mechanics-A/Solids* 40, 11-33.
- Crosson, R., Lin, J.-W. 1971. Voigt and Reuss prediction of anisotropic elasticity of dunite. *J. Geophys. Res.* 76, 570-578.
- Cyprych, D., Piazzolo, S., Almqvist, B.S.G. 2017. Seismic anisotropy from compositional banding in granulites from the deep magmatic arc of Fiordland, New Zealand. *Earth. Planet. Sci. Lett.* 477, 156-167.
- Deer, W.A., Howie, R.A., Zussman, J. 2013. *An Introduction to the Rock-Forming Minerals*. 3rd Edition, Berfords Information Press, Stevenage, Hertfordshire, UK, 498 pp.
- Dempsey, E.D., Prior, D., Mariotti, E., Toy, V.G. 2011. Mica-controlled anisotropy within mid-to-upper crustal mylonites: an EBSD study of mica fabrics in the Alpine Fault Zone, New Zealand. *Geol. Soc. London Spec. Pub.* 360, 33-47.
- Elger, J., Berndt, C., Kästner, F., Pierdominici, S., Kück, J., Almqvist, B.S.G., Juhlin, C., Lorenz, H. 2021. Core-log-seismic integration in metamorphic rocks and its implication for the regional geology: A case study for the ICDP drilling project COSC-1, Sweden. *Geochem. Geophys. Geosys.*, doi:10.1029/2020GC009376.
- Erdman, M.E., Hacker, B.R., Zandt, G., Seward, G. 2013. Seismic anisotropy of the crust: electron-backscatter diffraction measurements from the Basin and Range. *Geophys. J. Int.* doi:10.1093/gji/ggt287.
- Fliervoet, T.F., White, S.H., Drury, M.R. 1997. Evidence for dominant grain-boundary sliding deformation in greenschist- and amphibolite-grade polymineralic ultramylonites from the Redbank Deformed Zone, Central Australia. *J. Struct. Geol.* 19, 1495-1520.

- Fossen, H., Cavalcante, G.C.G. 2017. Shear zones – a review. *Earth-Sci. Rev.* 171, 434-455.
- Frederiksen, S., Braun, J. 2001. Numerical modelling of strain localisation during extension of the continental lithosphere. *Earth Planet. Sci. Lett.* 188, 241-251.
- Gee, D.G. 1975. A tectonic model for the central part of the Scandinavian Caledonides. *Am. J. Sci.* 275A, 468-515.
- Gee, D.G. 1978. Nappe displacement in the Scandinavian Caledonides. *Tectonophysics* 47, 393-399.
- Gee, D., Juhlin, C., Pascal, C., Robinson, P. 2010. Collisional Orogeny in the Scandinavian Caledonides (COSC). *Geologiska Föreningen i Stockholm Förhandlingar* 132, 29-44.
- Gueydan, F., Précigout, J., Montési, L.G.J. 2014. Strain weakening enables continental plate tectonics. *Tectonophysics* 631, 189-196.
- Hacker B.R. Ritzwoller, M.H., Xie, J. 2014. Partially melted, mica-bearing crust in Central Tibet. *Tectonics* 33, 1408-1424, doi:10.1002/2014TC003545.
- Han, S., Jung, H. 2021. Deformation Microstructures of Phyllite in Gunsan, Korea, and Implications for Seismic Anisotropy in Continental Crust. *Minerals*, 11(3), 294.
- Hedin, P., Juhlin, C., Gee, D.G. 2012. Seismic imaging of the Scandinavian Caledonides to define ICDP drilling sites. *Tectonophysics* 554-557, 3-41.
- Hedin, P., Malehmir, A., Gee, D.G., Juhlin, C., Dyrelius, D. 2014. 3D interpretation by integrating seismic and potential field data in the vicinity of the proposed COSC-1 drill site, central Swedish Caledonides. *Geol. Soc., London Spec. Pub.* 390, 301-319.
- Hedin, P., Almqvist, B.S.G., Berthet, T., Juhlin, C., Buske, S., Simon, H., Giese, R., Krauss, F., Rosberg, J.-E., Alm, P.G. 2016. 3D reflection seismic imaging at the 2.5 km deep COSC-1 scientific borehole, central Scandinavian Caledonides. *Tectonophysics* 689, 40-55.
- Hielscher, R. Schaeben, H. 2008. A novel pole figure inversion method: specification of the *MTEX* algorithm. *J. Applied Crystallography* 41, 1024-1037.
- Hirn, A., Damotte, B., Torrellis, ECORS Scientific Party. 1987. Crustal reflection seismics: the contributions of oblique, low frequency and shear wave illuminations. *Geophys. J. Int.*, 89, 287-296.
- Hirth, G., Tullis, J. 1992. Dislocation creep regimes in quartz aggregates. *J. Struct. Geol.* 14, 145-159.

- Hobbs, B.E., Ord, A., Teyssier, C. 1986. Earthquakes in the ductile regime? *Pure App. Geophys.* 124, 309-336.
- Holmberg, J. 2017. Pressure-temperature-time constraints on the deep subduction of the Sveco-Nappe Complex in Jämtland and southern Västerbotten, Scandinavian Caledonides. MSc Thesis, Uppsala University, 85pp.
- Hu, N., Li, Y., Xu, L. 2020. Crustal seismic anisotropy of the Northeastern Tibetan Plateau and the adjacent areas from shear-wave splitting measurements. *Geophys. J. Int.* 220, 1491-1503.
- Humbert, P., Plique, F. 1972. Propriétés élastiques de carbonate rhomboédriques monocristallines: calcite, magnésite, dolomie. *Comptes Rendus de l'Académie des Sciences Paris, Serie B*, 275, 391–394.
- Ji, S., Mainprice, D. 1988. Natural deformation fabrics of plagioclase : implications for slip systems and seismic anisotropy. *Tectonophysics* 147, 145-163.
- Ji, S., Salisbury, M. 1993a. Shear-wave velocities, anisotropy and splitting in the high grade mylonites. *Tectonophysics* 221, 3/4, 453-471.
- Ji, S., Salisbury, M., Hanmer, S. 1993b. Petrofabric, P-wave anisotropy and seismic reflectivity of high grade tectonites. *Tectonophysics*, 222, 195-226.
- Ji, S., Shao, T., Michibayashi, K., Long, C., Wang, Q., Kondo, Y., Zhao, W., Wang, H., Salisbury, M. H. 2013. A new calibration of seismic velocities, anisotropy, fabrics, and elastic moduli of amphibole rich rocks. *J. Geophys. Res.: Solid Earth* 118, no. 9, p. 4699-4728.
- Ji, S., Shao, T., Michibayashi, K., Oya, S., Satsukawa, T., Wang, Q., Zhao, W., Salisbury, M.H. 2015. Magnitude and symmetry of seismic anisotropy in mica- and amphibole-bearing metamorphic rocks and implications for tectonic interpretation of seismic data from southeast Tibetan Plateau. *J. Geophys. Res.* 120, doi:10.1002/2015012209.
- Jiang, D.Z., Williams, P.F. 1998. High-strain zones: a unified model. *J. Struct. Geol.* 20, 1105-1120.
- Jiang, F., Speziale, S., Duffy, T.S. 2004. Single-crystal elasticity of grossular- and almandine-rich garnets to 11 GPa by Brillouin scattering. *J. Geophys. Res.* 109, B10210, doi:10.1029/2004JB002081.

- Jones, T.D., Nur, A. 1984. The nature of seismic reflections from deep crustal fault zones. *J. Geophys. Res.* 89, 3153-3171.
- Jung, H. 2017. Crystal preferred orientations of olivine, orthopyroxene, serpentine, chlorite, and amphibole, and implications for seismic anisotropy in subduction zones: a review. *Geosciences Journal* 21, 985-1011.
- Khazanehdari, J., Rutter, E.H., Casey, M., Burlini, L. 1998. The role of crystallographic fabric in the generation of seismic anisotropy and reflectivity of high strain zones in calcite rocks. *J. Struct. Geol.* 20, 293-299.
- Kim, J., Jung, H. 2019. New crystal preferred orientation (CPO) of amphibole experimentally found in simple shear. *Geophys. Res. Lett.* 46, doi:10.1029/2019GL085189.
- Kim, J., Jung, H. 2020. Lattice Preferred Orientation (LPO) and Seismic Anisotropy of Amphibole in Gapyeong Amphibolites. *Korean Journal of Mineralogy and Petrology* 33, 259-272.
- Klonowska, I., Majka, J., Janák, M., Gee, D.G., Madenberger, A. 2014. Pressure-temperature evolution of a kyanite-garnet pelitic gneiss from Åreskutan: evidence of ultra-high-pressure metamorphism of the Seve Nappe Complex, west-central Jämtland, Swedish Caledonides. *Geol. Soc. London Spec. Pub.* 390, 321-336.
- Ko, B., Jung, H. 2015. Crystal preferred orientation of an amphibole experimentally deformed by simple shear. *Nat. Comm.* 6:6586, doi:10.1038/ncomms7586.
- Kronenberg, A.K., Kirby, S.H., Finkston, J. 1990. Basal slip and mechanical anisotropy of biotite. *J. Geophys. Res.*, 95, 19257-19278.
- Kruse, R., Stünitz, H. 1999. Deformation mechanisms and phase distribution in mafic high-temperature mylonites from the Jotun Nappe, southern Norway. *Tectonophysics* 303, 223-249.
- Kästner, F., Pierdominici, S., Elger, J., Zappone, A., Kück, J., Berndt, C. 2020. Correlation of core and downhole seismic velocities in high-pressure metamorphic rocks: a case study for the COSC-1 borehole, Sweden. *Solid Earth* 11, 607-626, doi:10.5194/se-11-607-2020.
- Kästner, F., Pierdominici, S., Zappone, A., Morales, L.F.G., Schleicher, A.M., Wilke, F.D.H., Berndt, C. 2021. Cross-scale seismic anisotropy analysis in metamorphic rocks from the COSC-1 borehole in the Scandinavian Caledonides. *Journal of Geophysical Research* 126, e2020JB021154. doi:10.1029/2020JB021154.

- Labrousse, L., Hetényi, G., Raimbourg, H., Jolivet, L., Andersen, T.B. 2010. Initiation of crustal-scale thrusts triggered by metamorphic reactions at depth: Insights from a comparison between the Himalayas and Scandinavian Caledonides. *Tectonics* 29, TC5002, doi:10.1029/2009TC002602.
- Lakshtanov, D.L., Sinogeikin, S.V., Bass, J.D. 2007. High-temperature phase transitions and elasticity of silica polymorphs. *Phys. Chem. Min.* 34, 11-22.
- Law, R. D., Schmid, S. M., Wheeler, J. 1990. Simple shear deformation and quartz crystallographic fabrics: a possible natural example from the Torridon area of NW Scotland. *J. Struct. Geol.* 12(1), 29-45.
- Law, R., Searle, M.P., Godin, L. 2006. Channel flow, ductile extrusion and exhumation in continental collision zones. *Geol. Soc. London, Spec. Pub. 268*, Geological Society Publishing House, 620 pp.
- Lee, A.L., Walker, A.M., Lloyd, G.E., Torvela, T. 2016. Modeling the impact of melt on seismic properties during mountain building. *Geochim. Geophys. Geosys.* doi:10.1002/2016GC006705.
- Liu, Y., Schmitt, D.R. 2006. The transition between the scale domains of Ray and Effective medium theory and anisotropy: numerical models. *Pure Appl. Geophys.* 163, 1327-1349.
- Lloyd, G.E., Kendall, J.-M. 2005. Petrofabric-derived seismic properties of a mylonitic quartz simple shear zone: Implications for seismic reflection profiling. *Geol. Soc. London Spec. Pub.* 240, 75-94
- Lloyd, G.E., Butler, R.W.H., Casey, M., Tatham, D.J., Mainprice, D. 2011. Constraints on the seismic properties of the middle and lower continental crust. *Geol. Soc. London Spec. Pub.* 260, 7-32.
- Lloyd, G., Butler, R.W.H., Casey, M., Mainprice, D. 2009. Mica, deformation fabrics and the seismic properties of the continental crust. *Earth Planet. Sci. Lett.* 288, 320-328.
- Mahan, K. 2006. Retrograde mica in deep crustal granulites: Implications for crustal seismic anisotropy. *Geophys. Res. Lett.* 33, doi:10.1029/2006GL028130.
- Mainprice, D. 1990. A FORTRAN program to calculate seismic anisotropy from the lattice preferred orientation of minerals. *Comp. Geosci.* 16, 385-393.

- Mainprice, D. 2007. Seismic anisotropy of the deep Earth from a mineral and rock physics perspective. Schubert, G. (ed), *Treatise on Geophysics*, vol. 2, 437-492.
- Mainprice, D., Nicolas, A., 1989. Development of shape and lattice preferred orientations: application to the seismic anisotropy of the lower crust. *J. Struct. Geol.* 11, 175-189.
- Mainprice, D., Bouchez, J.-L., Blumenfeld, P., Tubià, J.M. 1986. Dominant *c* slip in naturally deformed quartz: Implications for dramatic plastic softening at high temperature. *Geology* 14, 819-822.
- Majka, J., Be'eri-Schlevin, Y., Gee, D.G., Ladenberger, A., Claesson, S., Konečný, P., Klonowska, I. 2012. Multiple monazite growth in the Åreskutan migmatite: evidence for a polymetamorphic Late Ordovician to Late Silurian evolution in the Seve Nappe Complex of west-central Jämtland, Sweden. *J. Geosci.* 57, 3-23.
- Marion, D., Mukerji, T., Mavko, G. 1994. Scale effects on velocity dispersion: From ray to effective medium theories in stratified media. *Geophysics* 59, 1613-1619.
- Montési, L.G.J. 2013. Fabric development as the key for forming ductile shear zones and enabling plate tectonics. *J. Struct. Geol.* 50, 254-266.
- Naus-Thijssen, F.M.J., Goupee, A.J., Vel, S.S., Johnson, S.E. 2011. The influence of microstructure on seismic wave speed anisotropy in the crust: computational analysis of quartz-muscovite rocks. *Geophys. J. Int.* 185, 609-621, doi:10.1111/j.1365-246X.2011.04978.x.
- Okaya, D., Vel, S.S., Song, W.J., Johnson, S.E. 2019. Modification of crustal seismic anisotropy by geological structures (« structural geometric anisotropy »). *Geosphere*, 15, 146-170.
- Paaschier, C.W., Trouw, R.A.J. 2005. *Microtectonics*. Springer-Verlag Berlin Heidelberg, Germany, 366 pp.
- Piazolo, S., Passchier, C. W. 2002. Controls on lineation development in low to medium grade shear zones: a study from the Cap de Creus peninsula, NE Spain. *J. Struct. Geol.* 24(1), 25-44.
- Piazolo, S., Daczko, N. R., Silva, D., Raimondo, T. 2020. Melt-present shear zones enable intracontinental orogenesis. *Geology*, 48(7), 643-648.

- Platt, J. P., Behrmann, J. H. 1986. Structures and fabrics in a crustal-scale shear zone, Betic Cordillera, SE Spain. *J. Struct. Geol.*, 8(1), 15-33.
- Poirer, J.P. 1980. Shear localization and shear instability in materials in the ductile field. *J. Struct. Geol.* 2, 135-142.
- Raimondo, T., Clark, C., Hand, M., Faure, K. 2011. Assessing the geochemical and tectonic impacts of fluid–rock interaction in mid-crustal shear zones: a case study from the intracontinental Alice Springs Orogen, central Australia. *J. Metamorph Geol.*, 29(8), 821-850.
- Ramsay, J.G. 1980. Shear zone geometry: A review. *J. Struct. Geol.* 2, 83-99.
- Rey, P., Fountain, D.M., Clement, W.P. 1994. P wave velocity across a noncoaxial ductile shear zone and its associated strain gradient: Consequences for upper crustal reflectivity. *J. Geophys. Res.* 99, 4533-4548.
- Ryzhova, T.V., Aleksandrov, K.S., Korobkova, V.M. 1955. The elastic properties of rock-forming minerals V. Additional data on silicates. *Izv. Earth Phys.*, 2, 63-65.
- Satsukawa, T., Ildefonse, B., Mainprice, D., Morales, L.F.G., Michibayashi, K., Barou, F. 2013. A database of plagioclase crystal preferred orientations (CPO) and microstructures – implications for CPO origin, strength, symmetry and seismic anisotropy in gabbroic rocks. *Solid Earth* 4, 511-542.
- Schulte-Pelkum, V., Mahan, K. 2014. Imaging faults and shear zones using receiver functions. *Pure Appl. Geophys.* 171, 2967-2991.
- Schulte-Pelkum, V., Monaldi, G., Sheehan, A., Pandey, M.R., Sapkota, S., Bilham, R., Wu, F. 2005. Imaging the Indian subcontinent beneath the Himalaya. *Nature* 435, 1222-1225, doi:10.1038/nature03678.
- Selverstone, J., Morteani, G., Staude, J. M. 1991. Fluid channelling during ductile shearing: transformation of granodiorite into aluminous schist in the Tauern Window, Eastern Alps. *J. Metamorphic Geol.* 9(4), 419-431.
- Sha, M.C., Li, Z. 1994. Single-crystal elastic constants of fluorapatite, $\text{Ca}_5\text{F}(\text{PO}_4)_3$. *J. App. Phys.* 75, 7784, doi:10.1063/1.357030.

- Sharma, A., Baruah, S., Piccinini, D., Saikia, S., Phukan, M.K., Chetia, M., Kayal, J.R. 2017. Crustal seismic anisotropy beneath Shillong plateau – Assam valley in North East India: Shear-wave splitting analysis using local earthquakes. *Tectonophysics* 717, 425-432.
- Shao, T., Ji, S., Oya, S., Michibayashi, K., Wang, Q. 2016. Mica-dominated seismic properties of mid-crust beneath west Yunnan (China) and geodynamic implications. *Tectonophysics* 677-678, 324-338.
- Shapiro, N.M., Ritzwoller, M.H., Molnar, P., Levin, V. 2004. Thinning and flow of Tibetan crust constrained by seismic anisotropy. *Science* 305, 233-236.
- Simon, H., Buske, S., Krauss, F., Giese, R., Hedin, P., Juhlin, C. 2017. The derivation of an anisotropic velocity model from a combined surface and bore hole seismic survey in crystalline environment at the COSC-1 borehole, central Sweden. *Geophys. J. Int.* 210, 1332-1346.
- Simon, H., Buske, S., Hedin, P., Juhlin, C., Krauss, F., Giese, R. 2019. Anisotropic Kirchhoff pre-stack depth migration at the COSC-1 borehole, central Sweden. *Geophys. J. Int.* 219, 66-79.
- Smithson, S. B., Brewer, J. A., Kaufman, S., Oliver, J. E., & Hurich, C. A. 1979. Structure of the Laramide Wind River Uplift, Wyoming, from Cocorp deep reflection data and from gravity data. *J. Geophys. Res.* 84(B11), 5955. <https://doi.org/10.1029/JB084iB11p05955>
- Stipp, M., Stünitz, H., Heilbronner, R., Schmid, S.M. 2002. The eastern Tonale fault zone: a ‘natural laboratory’ for crystal plastic deformation of quartz over a temperature range of 250 to 750 °C. *J. Struct. Geol.* 24, 1861-1884.
- Streule, M.J., Strachan, R A., Searle, M.P., Law, R.D. 2010. Comparing Tibet-Himalayan and Caledonian crustal architecture, evolution and mountain building processes. *Geol. Soc. London, Spec. Pub.* 335, 207-232.
- Sun, S., Ji, S., Wang, Q., Salisbury, M., Kern, H. 2012. P-wave velocity differences between surface-derived and core samples from the Sulu ultrahigh-pressure terrane: Implications for in situ velocities at great depths. *Geology* 40, 651-654.
- Svahnberg, H., Piazzolo, S. 2010. The initiation of strain localisation in plagioclase-rich rocks: Insights from detailed microstructural analyses. *J. Struct. Geol.* 32(10), 1404-1416.
- Tatham, D.J., Lloyd, G.E., Butler, G.W.H., Casey, M. (2008). Amphibole and lower crustal seismic properties. *Earth Planet. Sci. Lett.* 267, 118-128.

- Thybo, H., Youssef, M., Artemieva, I.M. 2019. Southern Africa crustal anisotropy reveals coupled crust-mantle evolution for over 2 billion years. *Nat. Comm.* 10, 5445.
- Toohill, K., Siegesmund, S., Bass, J.D. 1999. Sound velocities and elasticity of cordierite and implications for deep crustal seismic anisotropy. *Phys. Chem. Min.* 26, 333-343.
- Tsang, C.-F., Rosberg, J.-E., Sharma, P., Berthet, T., Juhlin, C., Niemi, A. 2016. Hydrologic testing during drilling: application of the flowing fluid electrical conductivity (FFEC) logging method to drilling of a deep borehole. *Hydrogeol. J.* doi:10.1007/s10040-016-1405z.
- Tullis, J., Snoke, A.W., Todd, V.R. 1982. Significance and petrogenesis of mylonitic rocks. *Geology* 10, 227-230.
- Vaucher, A., Tommasi, A., Mainprice, D. 2012. Faults (shear zones) in the Earth's mantle. *Tectonophysics* 558-559, 1-27.
- Vaughan, M.T., Weidner, D.J. 1978. The relationship of elasticity and crystal structure in andalusite and sillimanite. *Phys. Chemistry Min.* 3, 133-144.
- Vaughan, M.T., Guggenheim, S. 1986. Elasticity of muscovite and its relationship to crystal structure. *J. Geophys. Res.* 91, 4657-4664.
- Vel, S.S., Cook, A.C., Johnson, S.E., Gerbi, C. 2016. Computational homogenization and micromechanical analysis of texture of polycrystalline materials. *Computer Methods in Applied Engineering* 310, 749-779.
- Waeselmann, N., Brown, J.M., Angel, R.J., Ross, N., Zhao, J., Kaminsky, W. 2016. The elastic tensor of monoclinic alkali feldspar. *Am. Min.* 101, 1228-1231, doi:10.2138/am-2016-5583.
- Walker, A.M., Wookey, J.M. 2012. MSAT - a new toolkit for the analysis of elastic and seismic anisotropy. *Computers and Geosciences* 49, 81-90.
- Wang Q., Ji, S., Salisbury, M.H., Xia, B., Pan, M.B., Xu, Z.Q. 2005. Shear wave properties and Poisson's ratios of ultrahigh-pressure metamorphic rocks from the Dabie-Sulu orogenic belt: Implications for the crustal composition. *J. Geophys. Res.* 110, B08208, doi:10.1029/2004JB003435.
- Ward, D., Mahan, K., Schulte-Pelkum, V. 2012. Roles of quartz and mica in seismic anisotropy of mylonites. *Geophys. J. Int.* 190, 1123-1134, doi:10.1111/j.1365-246X.2012.05528.x.

- Weidner, D.J., Ito, E. 1985. Elasticity of MgSiO_3 in the ilmenite phase. *Phys. Earth Planet. Int.* 40, 65-70.
- Wenning, Q., Almqvist, B.S.G., Hedin, P., Zappone, A. 2016. Seismic anisotropy in mid to lower orogenic crust: Insights from laboratory measurements of V_p and V_s in drill core from central Scandinavian Caledonides. *Tectonophysics* 692, 14-28.
- White, S.H., Burrows, S.E., Carreras, J., Shaw, N.D., Humphreys, F.J. 1980. On mylonites in ductile shear zones. *J. Struct. Geol.* 2, 175-187.
- Whitney, D.L., Evans, B.W. 2010. Abbreviations for names of rock-forming minerals. *Am. Min.* 95, 185-187.
- Wrona, T., Fossen, H., Lecomte, I., Eide, C.H., Gawthorpe, R.L. 2020. Seismic expression of shear zones: Insights from 2-D point-spread-function based convolution modelling. *J. Struct. Geol.* 140, 104121, doi:10.1016/j.jsg.2020.104121.
- Zappone, A., Fernández, M., García-Duenas, V., Burdini, L. 2000. Laboratory measurements of seismic P-wave velocities on rocks from the Pyreneic chain (southern Iberian Peninsula). *Tectonophysics* 317, 259-272.

Journal Pre-proof

Credit Author Statement

Bjarne Almqvist (BA), Sandra Piazzolo (SP) and Daria Cyprych (DC) designed the study together. Samples were collected by DC and BA. Analytical work and measurement results were obtained by DC, BA and SP at Macquarie University. BA and DC prepared the first draft of the manuscript. All authors contributed to the concept of the article and editing of the manuscript.

Journal Pre-proof

Declaration of interests

The authors declare that they have no known competing financial interests or personal relationships that could have appeared to influence the work reported in this paper.

The authors declare the following financial interests/personal relationships which may be considered as potential competing interests:

Journal Pre-proof

Table 1. Summary of elastic stiffness tensors used and their source references

Elastic stiffness property files		
Mineral		Reference
Qtz	β -quartz	Lakshtanov et al. 2007
Pl	Albite	Brown et al. 2016
Kfs	Orthoclase	Waeselmann et al. 2016
Cal	Calcite	Chen et al. 2001
Dol	Dolomite	Humbert and Plique 1972
Hbl	#4 Hornblende - Tschermakite	Brown and Abramson 2016
Grt*	Pyrope	Chai et al. 1997
	Almandine	Jiang et al. 2004
	Andradite	
Di	Diopside (Di72He9Jd3Cr3Ts12)	Collins and Brown 1992
Bt	Biotite	Alexandrov and Ryzhova 1961
Ms	Muscovite	Vaughan & Guggenheim 1986
Sil	Sillimanite	Vaughan and Weidner 1978
Crd	Cordierite	Toohill et al. 1979
Ep	Epidote	Ryzhova et al. 1966
Ap	Apatite	Sha et al. 1994
Ilm	Ilmenite	Weidner and Ito 1985

Table 2. Modal abundance of minerals estimated based on EBSD analysis (area %) and calculated densities of analysed rock samples. Mineral abbreviations after Whitney and Evans (2010).

Rock type	Sample no.	Strain	Density (g/cm ³)	Qz	Pl	Kfs	Cal	Dol	Hbl	Grt*	Di	Bt	Ms	Sil	Crd
Marble	COSC13_007	M	2.70	12	1		87								
Marble	SC13_06C	H	2.71				100								
Calc-silicate	COSC_243	M	2.67	28	26		46								
Calc-silicate	COSC_47	M	2.74	6	38	20	20				13	3			
Calc-silicate	COSC13_006	M	2.67	35	19	22	15				4	1			
Calc-silicate	SC13_024	H	2.73	50	24		6	7	8			2	4		
Amphibolite	COSC13_001.2	M	3.10	5	25				70						
Amphibolite	COSC_149	M	3.04		38				58		3	2			
Amphibolite	COSC_193	M	3.11	3	25				72						
Amphibolite	COSC_556	H	3.13	4	20				75						
Hbl-gneiss	HL13_103	M	2.89	6	55				34			1			
Hbl-gneiss	COSC_631	H	3.07	3	11				84						
Qfs-gneiss	BQ2B	M	2.67	37	33	13	10				3	3			
Qfs-gneiss	BA13_V02	M	2.70	56	36						3				
Qfs-gneiss	COSC13_005A	M	2.64	40	33	24					2	1			
Qfs-gneiss	COSC_403	M	2.66	58	27	10					1	3			
Qfs-gneiss	SW14_01	H	2.79	44	24		5			5		16	6		
Bt-gneiss	BQ3	M	2.74	2	45	31	1				6	15			
Bt-gneiss	BQ7.2	M	2.70		37	46						18			

Quartzite	SW14_11	H?	2.67	71	20	2				3	4
Quartzite	SW14_02	H	2.68	83	4	9		4			
Quartzite	MH_09	H	2.74	84	2	7		6		1	
Quartzite	COSC_664	H	2.55	77	23						
Mica-schist	COSC_691	H	2.80	17	5						77

* Pyrope (SW14_02), Almandine (MH_09), Andradite (SW14_01)

Table 3. J-indices estimated for ODFs of major rock forming minerals (> 5 % area). All orientation data points are included. Mineral abbreviations after Whitney and Evans (2010)

Rock type	Sample no.	Strain	J-index								
			Qtz	Pl	Kfs	Cal	Dol	Hbl	Grt*	Di	
Marble	COSC13_007	M	1.5	16.8		2.1					
Marble	SC13_06C	H				5.0					
Calc-silicate	COSC_243	M	1.9	2.4		1.9					
Calc-silicate	COSC_487	M	1.3	1.6	1.7	1.5					3.7
Calc-silicate	COSC13_006	M	4.6	3.0	4.5	2.0					
Calc-silicate	SC13_08A	H	1.3	1.6		1.8	2.2	32.2			
Amphibolite	COSC13_001.2	M	1.6	1.8				4.5			
Amphibolite	COSC_149	M		1.7				2.3			3.3
Amphibolite	COSC_193	M	1.6	1.9				4.8			
Amphibolite	COSC_556	H	1.5	1.7				6.7			
Hbl-gneiss	HL13_103	M	1.6	2.8				5.5			
Hbl-gneiss	COSC_631	H	2.1	15.5				5.0			
Calc-silicate	BQ2B	M	2.2	2.7							2.9
Qfs-Gneiss	BA13_V02	M	5.2	1.6							43.4
Qfs-Gneiss	COSC13_005A	M	2.6	3.9	8.5						5.3
Qfs-Gneiss	COSC_403	M	4.4	2.9	2.0						5.3
Qfs-Gneiss	SW14_01	M	1.4	1.2		5.8				11.4	
Bt-gneiss	BQ3	M	1.4	2.0	2.9	3.5					6.1
Bt-gneiss	BQ7.2	M		2.1	2.9						
Quartzite	SW14_11	H?	7.6	10.7	13.3						
Quartzite	SW14_02	H	7.1	9.6	15.1					7.7	
Quartzite	MH_09	H	9.7	8.2	3.4					3.4	
Quartzite	COSC_664	H	3.3	1.9							
Mica-schist	COSC_691	H	1.5	3.8							

* Pyrope (SW14_02), Almandine (MH_09), Andradite (SW14_01)

Table 4. Densities, and P- and S-wave velocities and anisotropies calculated from the EBSD data and elastic constants using VRH average with AEH correction (AEH) and simple VRH average (VRH). Anisotropy is calculated using the formula $A = 200(V_{max} - V_{min}) / (V_{max} + V_{min})$. Mean VP = $(VP_{max} + VP_{min}) / 2$, Mean VS = $(VS1_{max} + VS2_{min}) / 2$.

Lithology	Sample	Strain	V _P				V _S		V _{S1}		
			Min	Max	Mean	A	Mean	MaxA	Min	Max	A

			(km/s)		(%)	(km/s)		%	(km/s)		(%)
Marble	COSC13_007	M	6.28	6.76	6.52	7.34	3.57	7.02	3.50	3.70	5.42
	SC13_06C	H	5.98	7.06	6.52	16.52	3.51	11.28	3.36	3.73	10.55
Calc-silicate	COSC_243	M	6.17	6.44	6.31	4.26	3.68	3.05	3.67	3.75	2.35
	COSC_487	M	6.38	6.62	6.50	3.73	3.68	4.22	3.65	3.77	3.21
	COSC13_006	M	6.13	6.46	6.29	5.28	3.77	3.85	3.74	3.86	3.13
	SC13_08A	H	6.05	6.47	6.26	6.68	3.92	8.82	3.80	4.09	7.40
Amphibolite	COSC13_001.2	M	6.38	7.11	6.74	10.83	4.01	8.80	3.85	4.19	8.31
	COSC_149	M	6.51	6.99	6.75	7.11	3.91	5.00	3.87	4.02	3.85
	COSC_193	M	6.44	7.15	6.80	10.46	4.00	8.25	3.84	4.16	7.92
	COSC_556	H	6.37	7.30	6.84	15.25	4.04	10.33	3.85	4.25	9.94
Hbl-gneiss	HL13_103	M	6.39	6.68	6.53	4.26	3.82	4.44	3.80	3.91	2.91
	COSC_631	H	6.44	7.33	6.39	13.00	3.76	8.27	3.64	3.92	7.33
Qfs-gneiss	BQ2B	M	6.10	6.37	6.24	4.30	3.76	4.02	3.76	3.84	1.92
	BA13_V02	M	6.12	6.44	6.28	5.16	3.96	4.55	3.94	4.07	3.22
	COSC13_005A	M	5.96	6.43	6.19	7.60	3.78	5.68	3.75	3.91	4.05
	COSC_403	M	5.91	6.36	6.13	7.27	3.87	9.17	3.85	4.05	5.22
	SW14_01	H	5.75	6.48	6.11	11.86	3.75	15.90	3.58	4.08	13.09
Bt-gneiss	BQ3	M	5.90	6.38	6.14	7.95	3.49	8.79	3.45	3.68	6.37
	BQ7(2)	M	5.75	6.29	6.02	8.96	3.38	12.54	3.24	3.60	10.73
Quartzite	SW14_11	M	5.74	6.33	6.03	9.78	3.91	12.77	3.87	4.17	7.32
	SW14_02	M	5.86	6.52	6.19	10.69	4.07	12.32	3.98	4.32	8.07
	MH_09	H	5.87	6.50	6.18	10.24	4.07	12.19	3.97	4.32	8.51
	COSC_664	H	5.90	6.30	6.10	6.49	3.99	7.02	3.96	4.13	4.13
Mica schist	COSC_657	H	5.12	7.02	6.07	31.37	3.70	34.27	3.19	4.34	30.67

Highlights

- * Seismic properties inferred for the Middle Allochthon rocks, Scandinavian Caledonides
- * Mineral modal composition and degree of strain control seismic anisotropy
- * The entire allochthonous nappe unit is predicted to be seismically anisotropic
- * AV_p ranges from 7-31 % and max AVs from 7-34 % in *high*-strain samples
- * AV_p ranges from 4-11 % and max AVs from 3-13 % in *medium*-strain samples

Journal Pre-proof

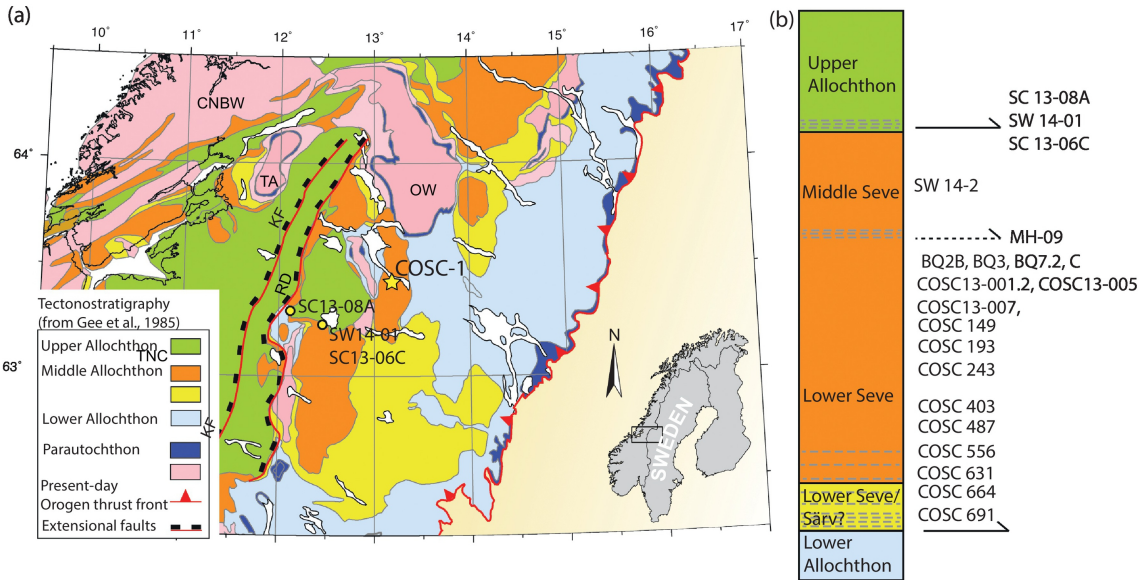


Figure 1

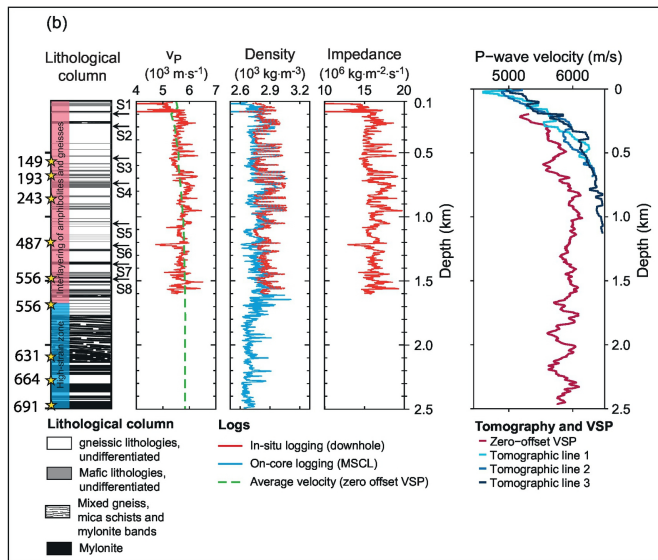
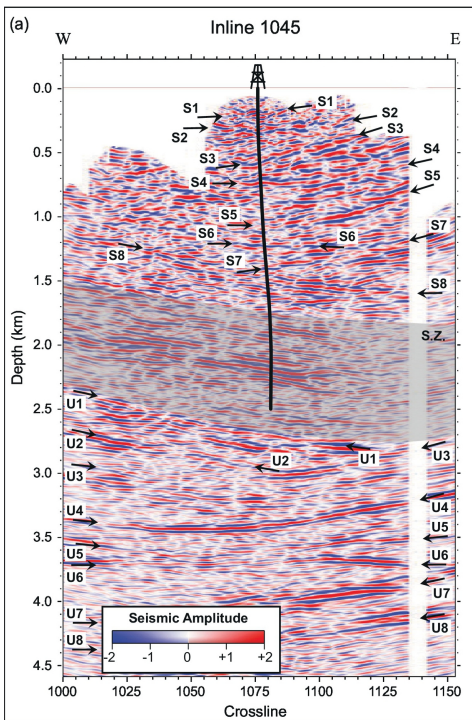


Figure 2



a



b



c

Figure 3

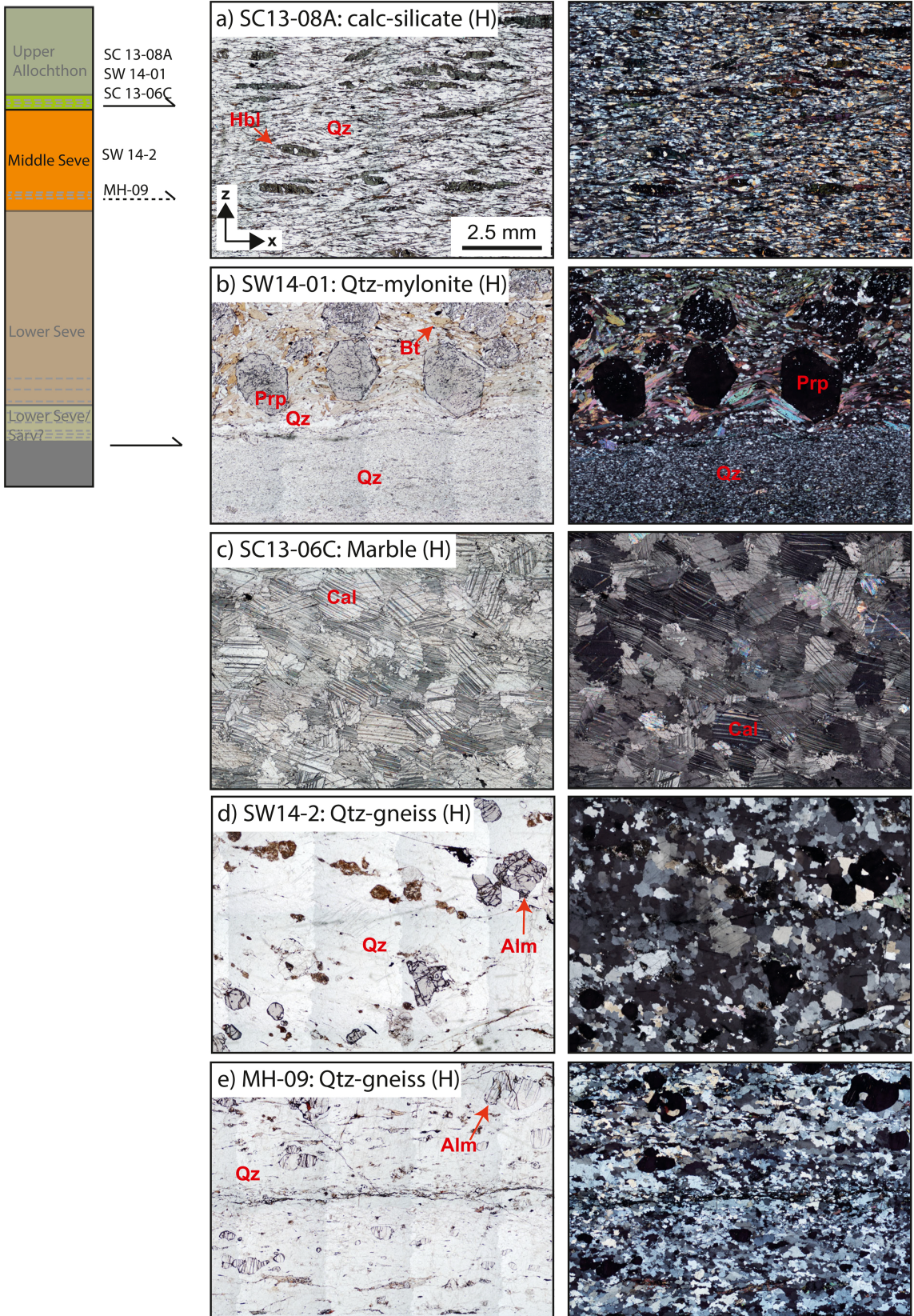


Figure 4

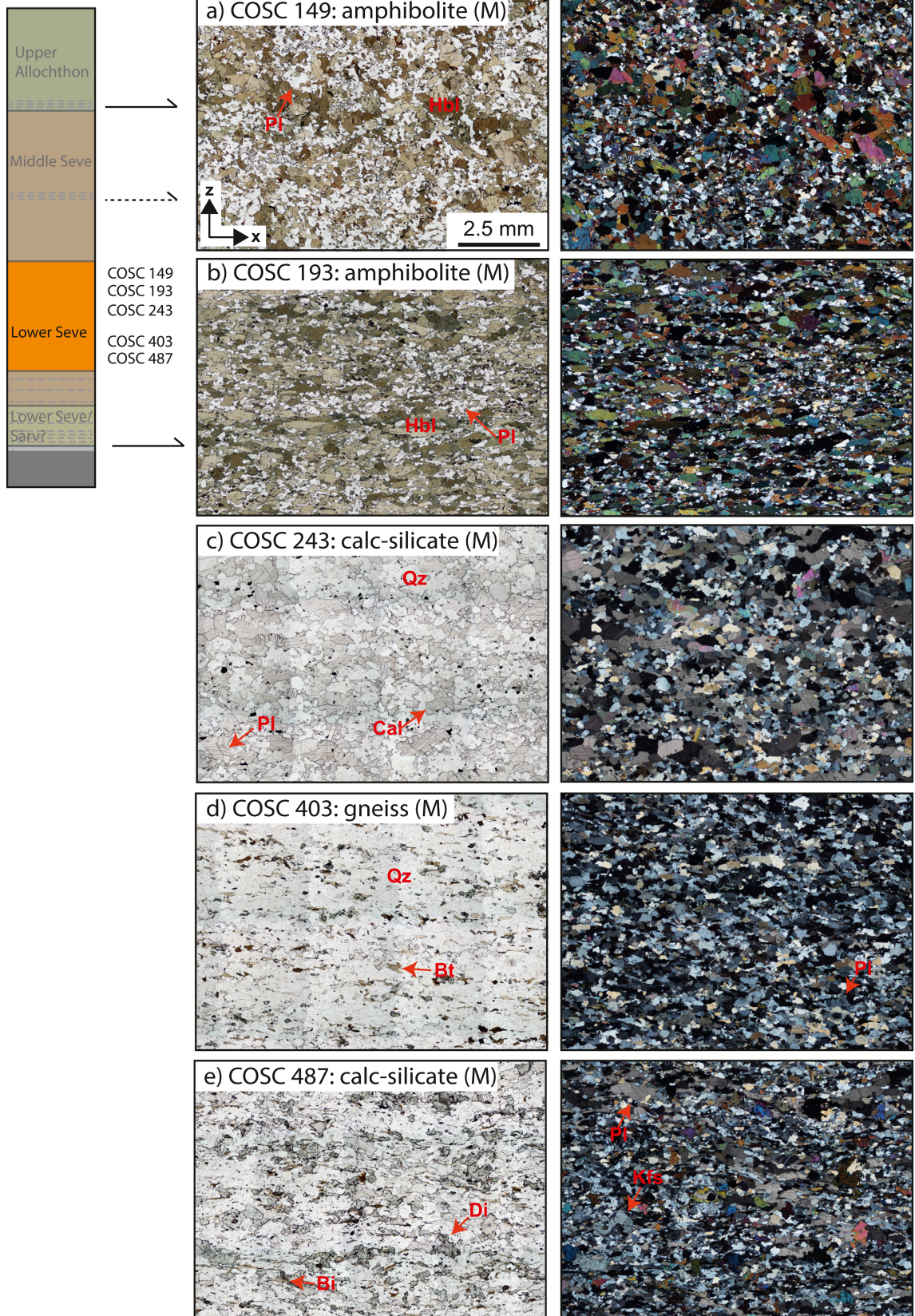


Figure 5

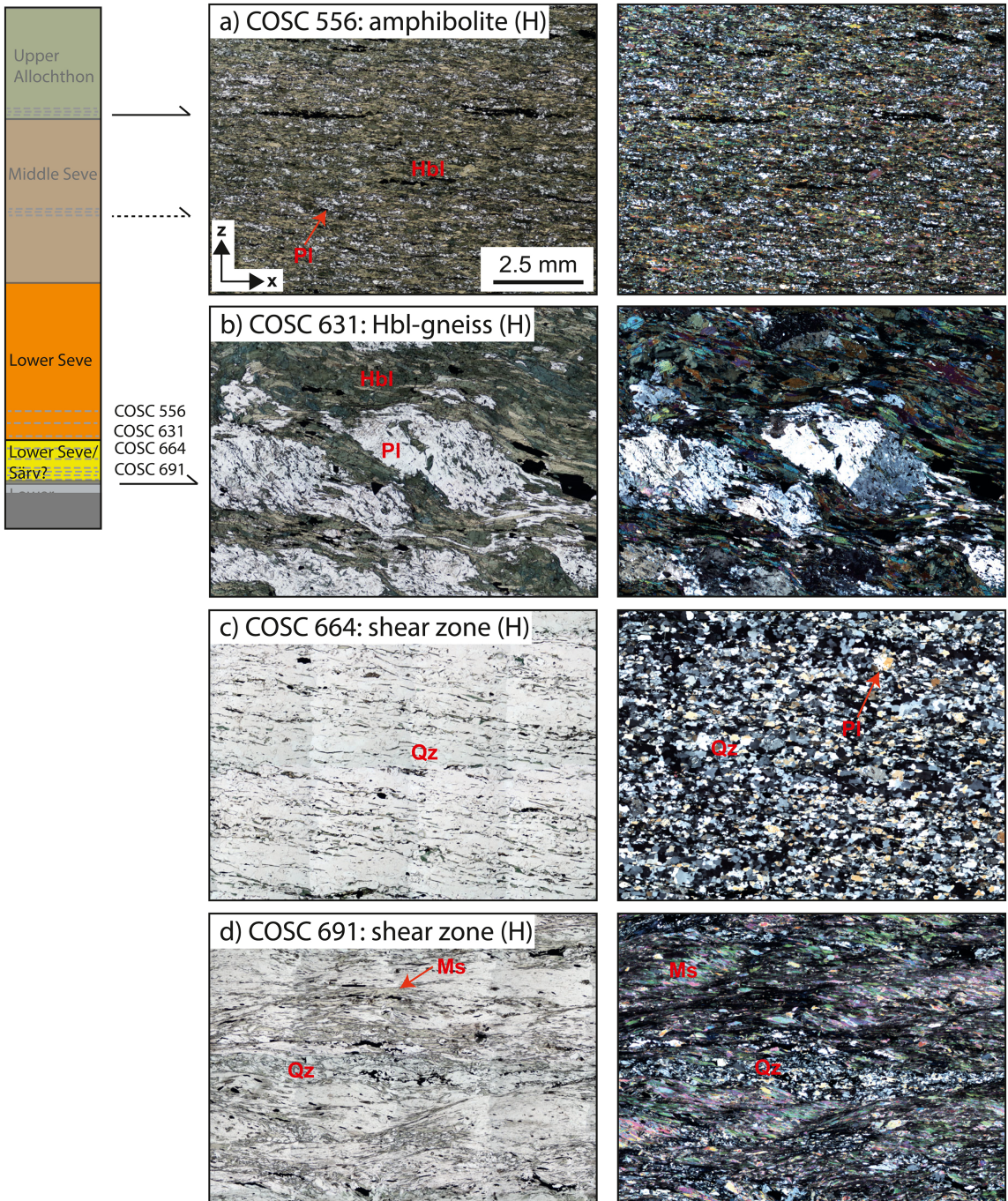


Figure 6

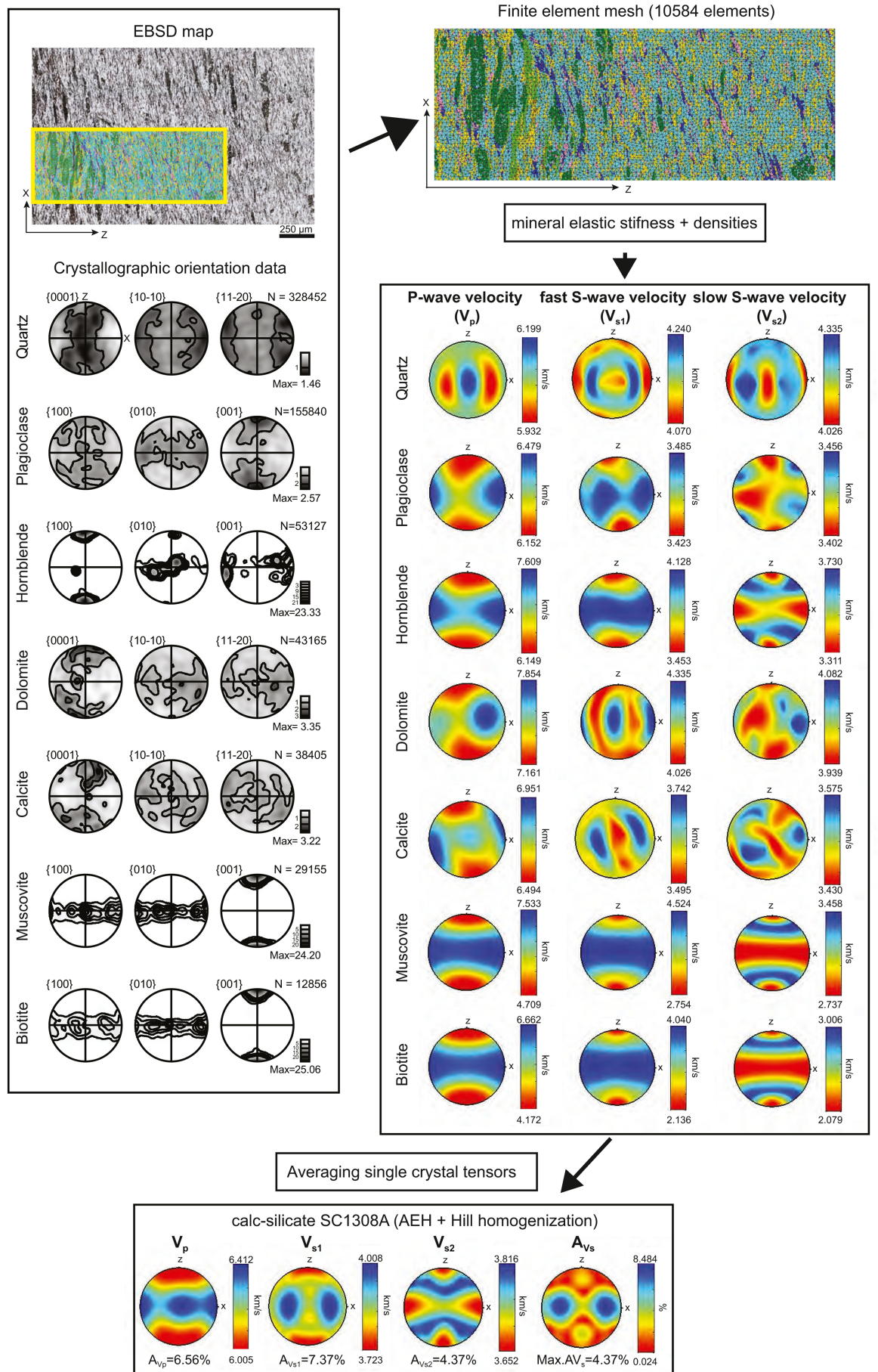


Figure 7

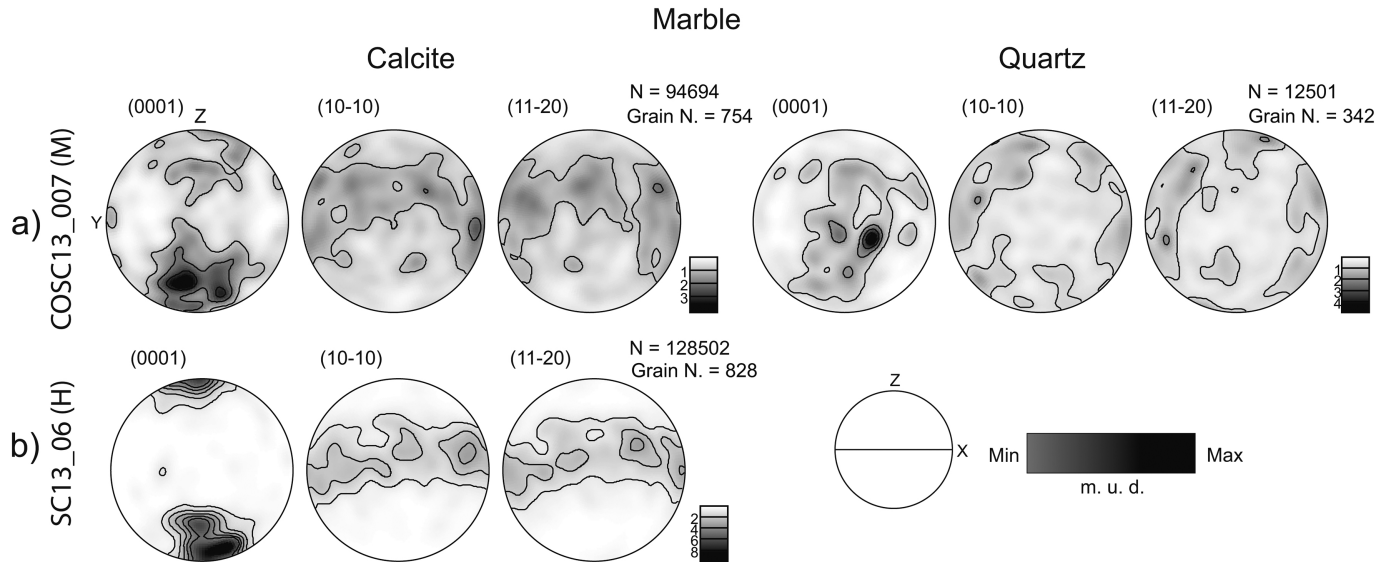


Figure 8

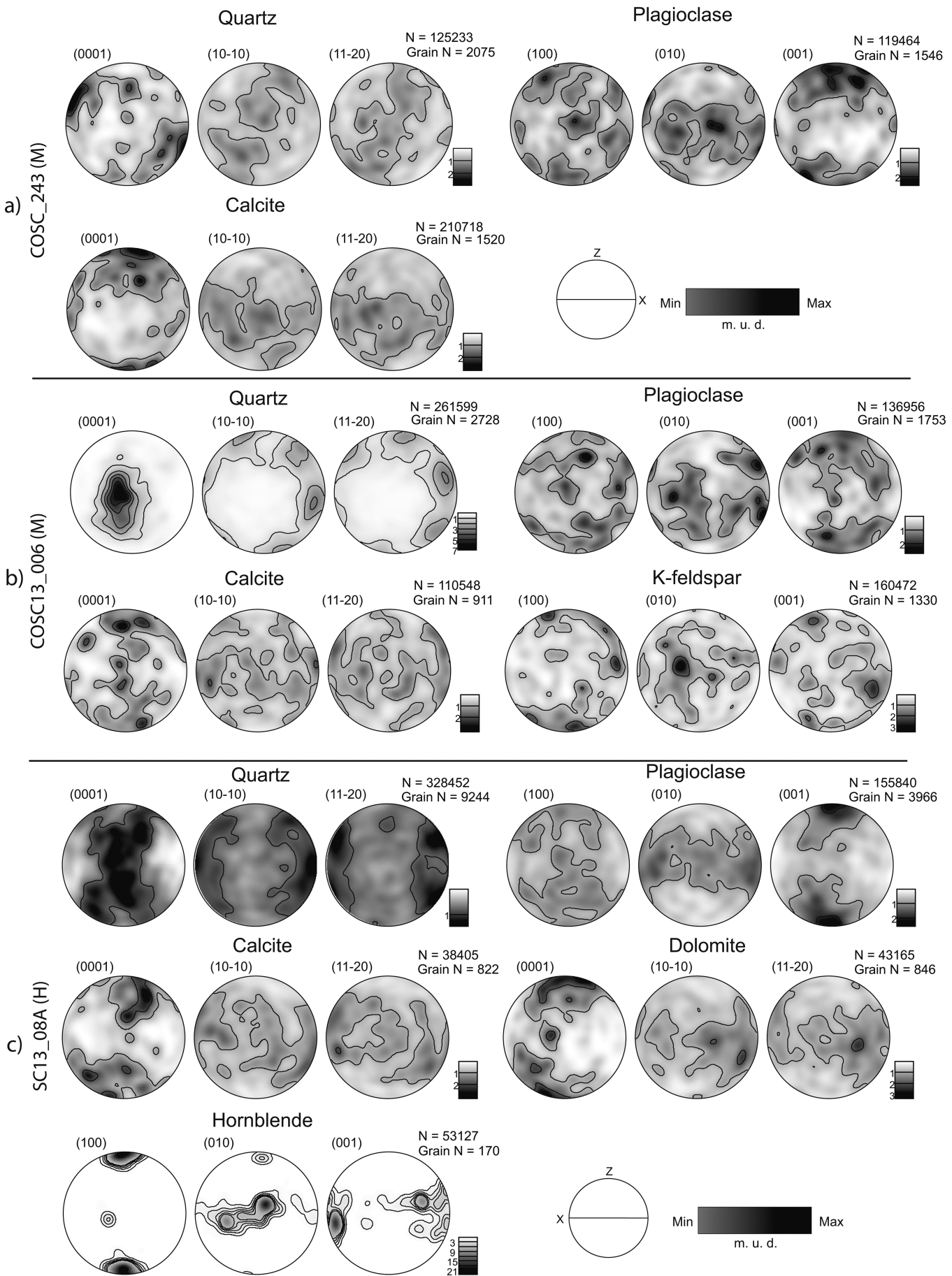


Figure 9

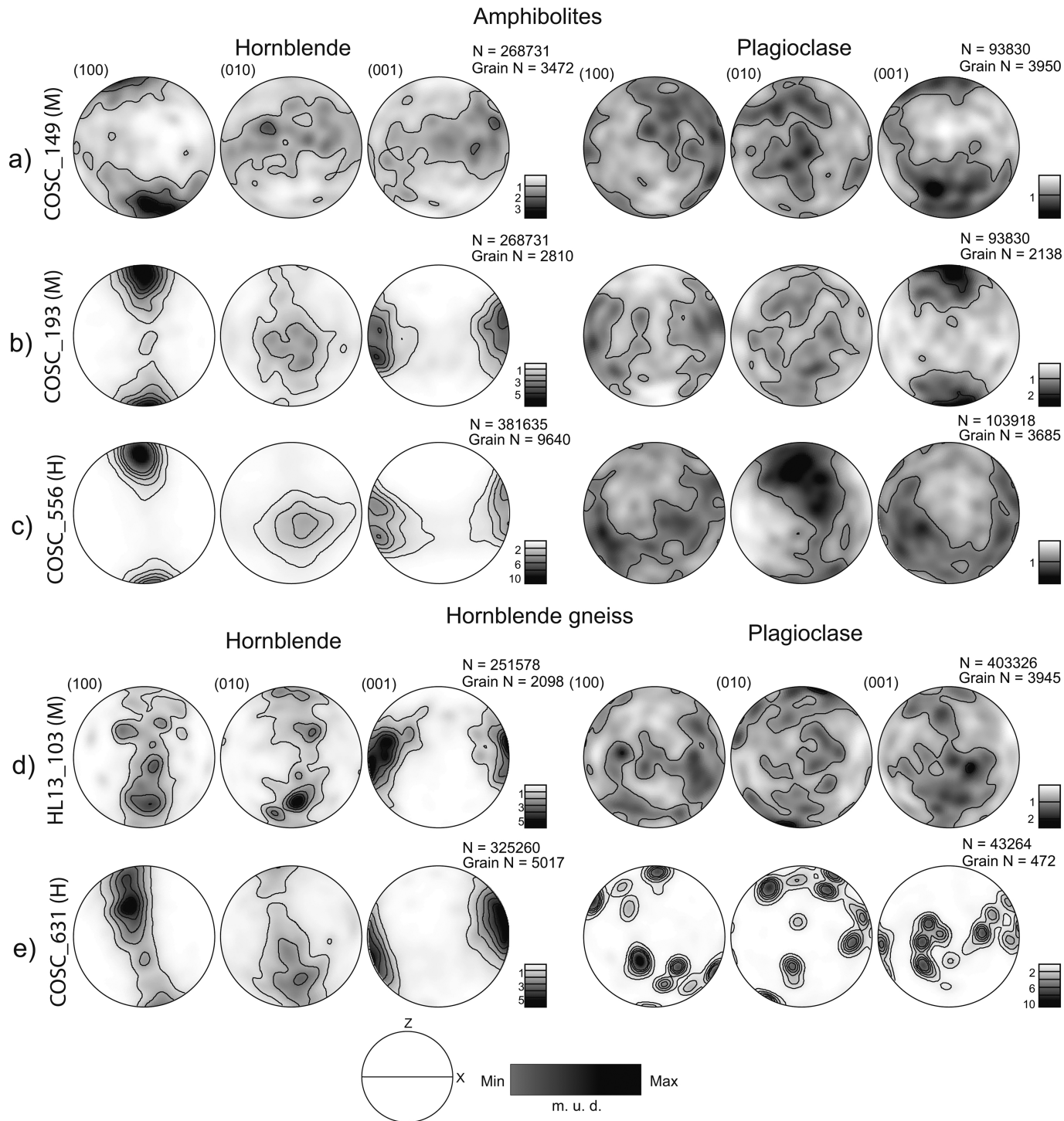


Figure 10

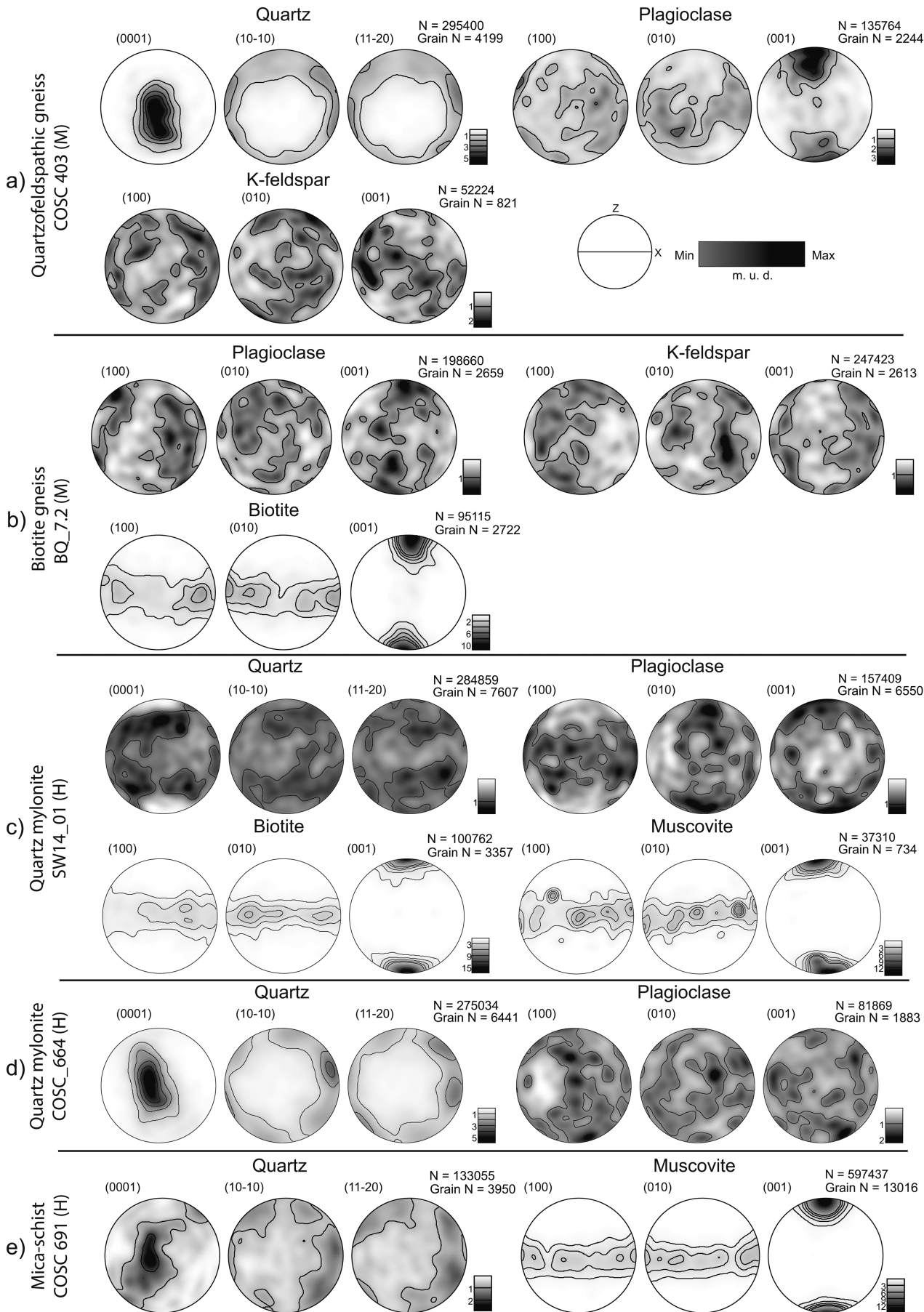


Figure 11: Equal area lower hemisphere pole figures showing CPO patterns of major rock forming minerals in gneisses with different compositions, for pole

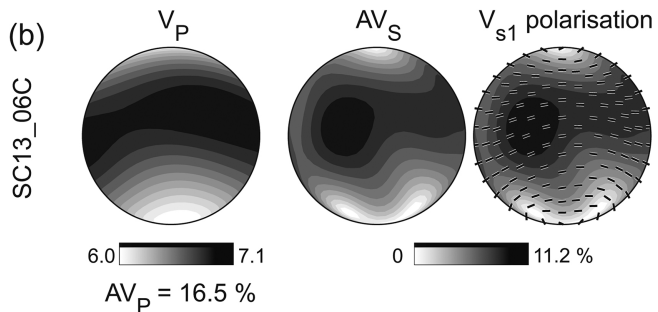
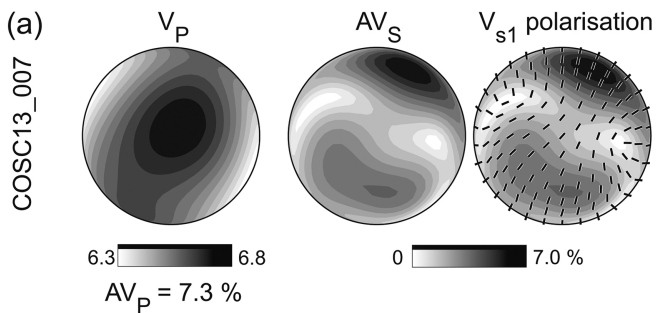
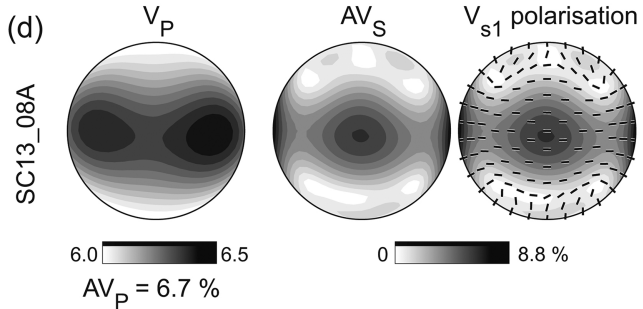
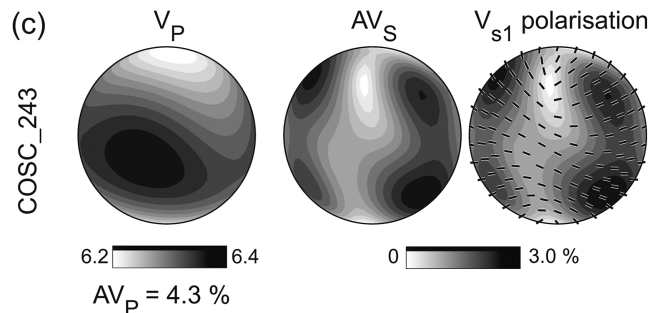
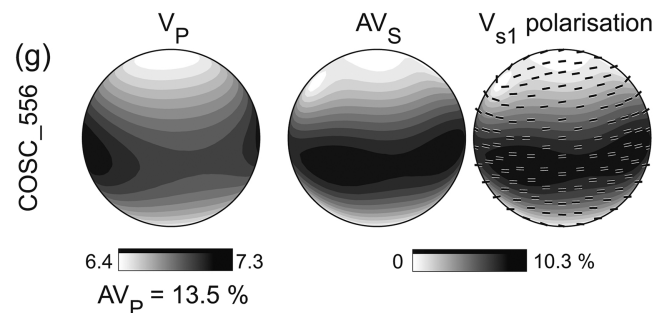
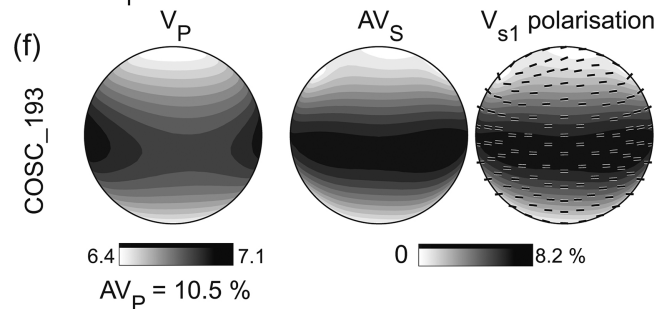
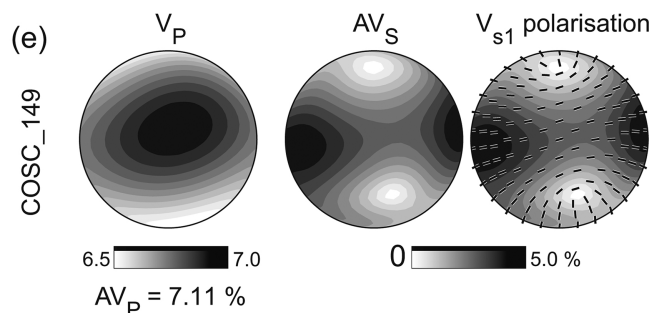
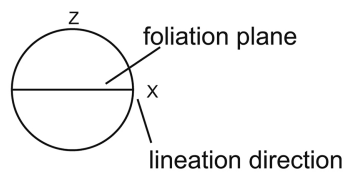
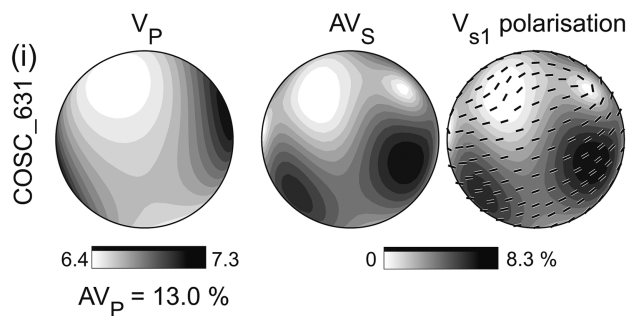
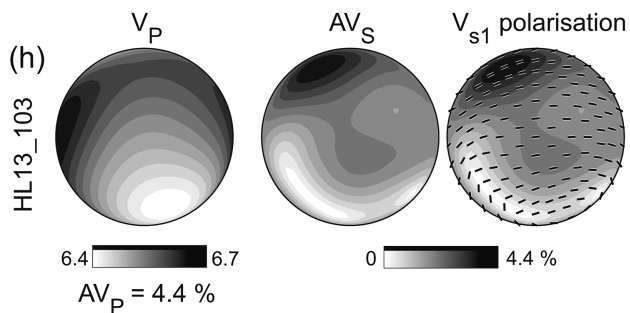
Marble**Calc-silicate****Amphibolite****Amphibole Gneiss**

Figure 12

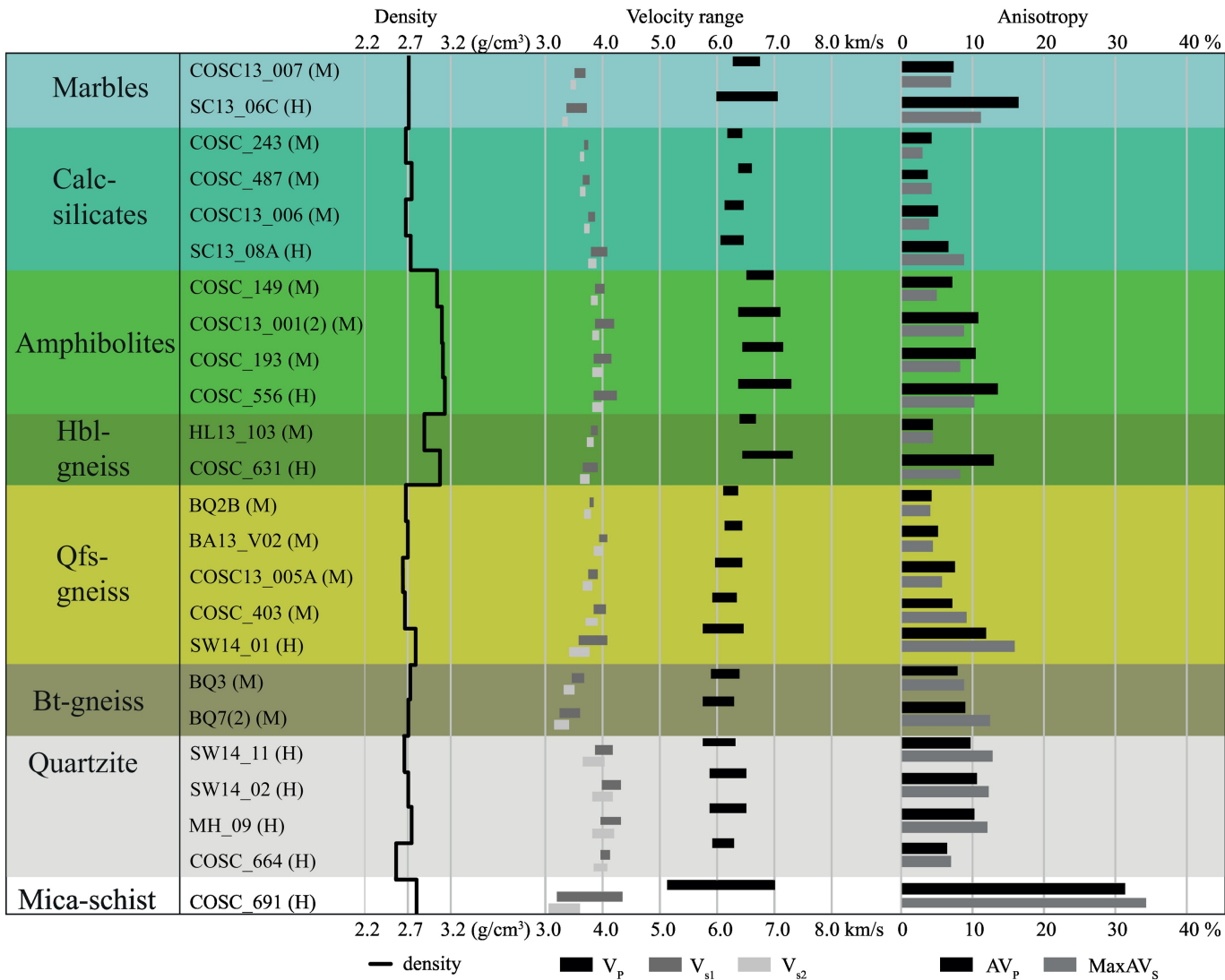


Figure 14

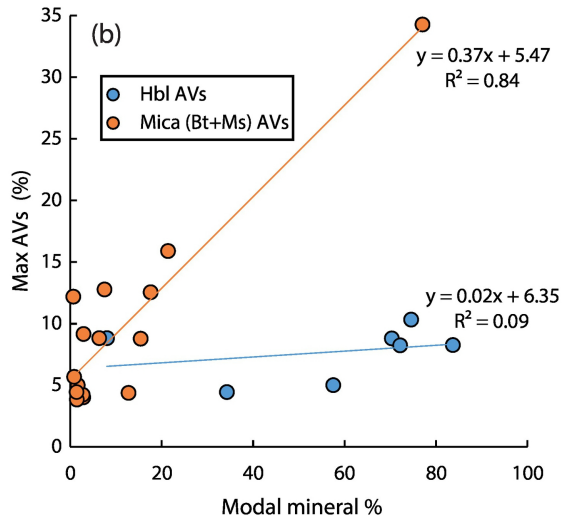
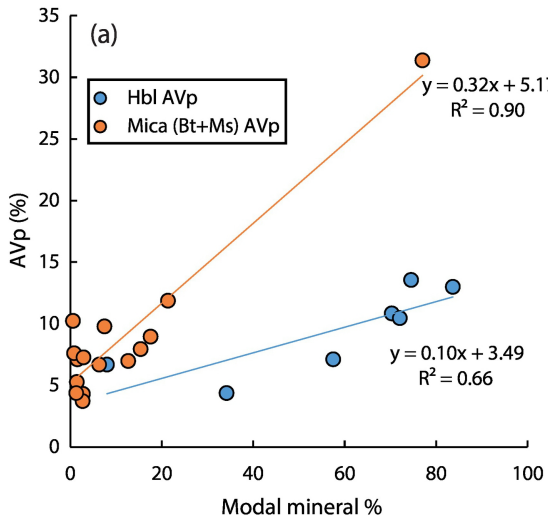


Figure 15

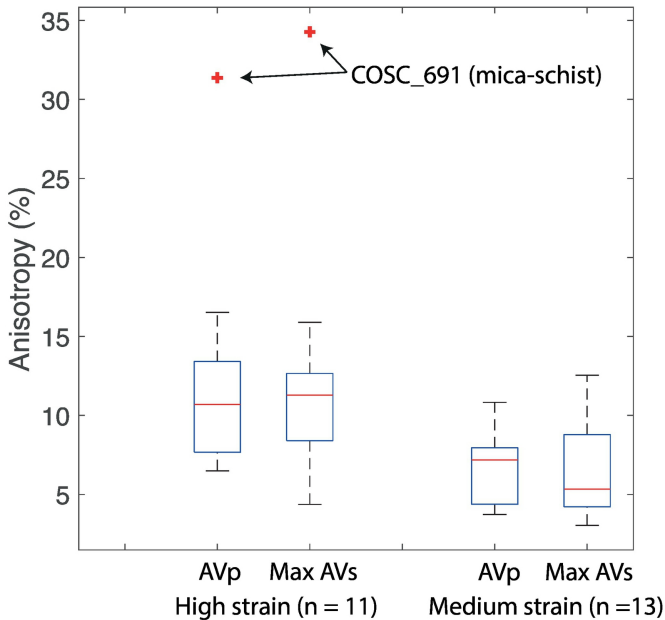


Figure 16

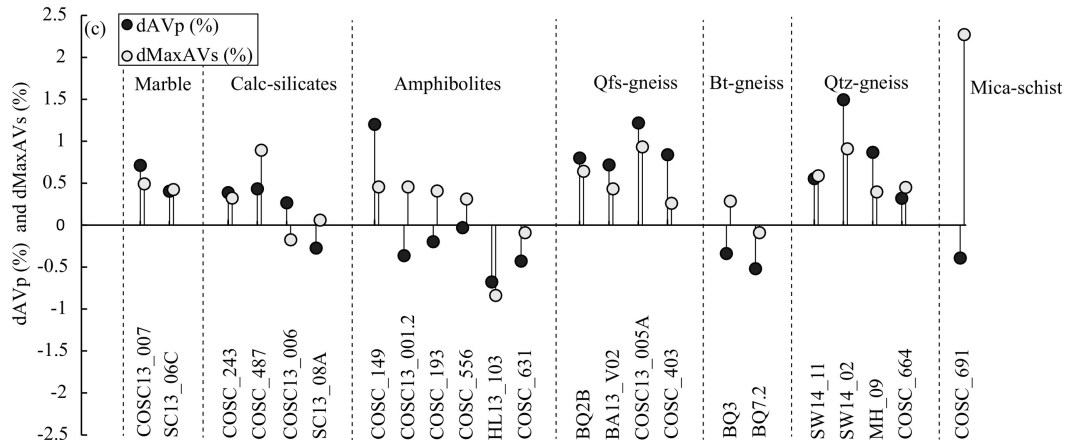
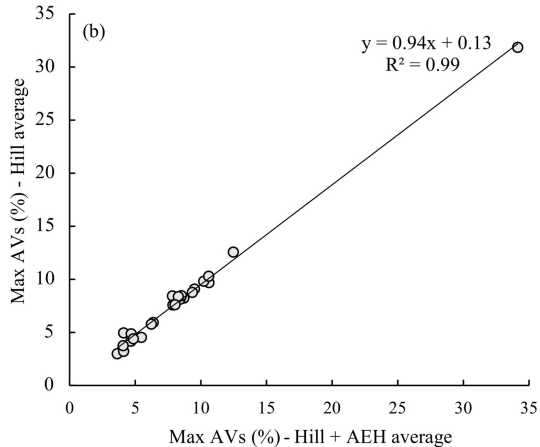
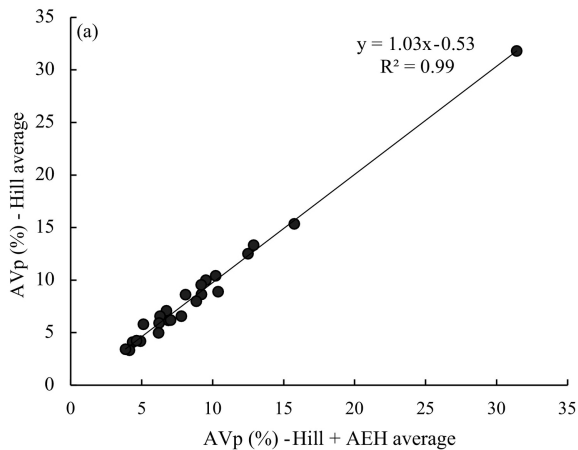


Figure 17

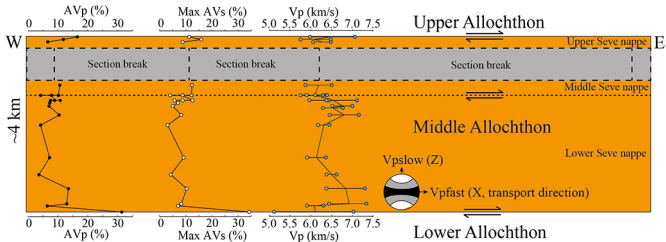


Figure 18